

7

The tropical route of QBO teleconnections in UKESM1 and HadGEM3

This chapter examines the influence of the stratospheric QBO on the tropical troposphere using, first, the results from the pre-industrial control experiments of CMIP6 of the MOHC models and then, targeted model experiments with nudging technique. The findings of this chapter are discussed in the context of existing hypotheses of physical mechanisms that could explain the downward tropical route of QBO influence.

7.1 Introduction

Long-distance effects or teleconnections associated with the stratospheric quasi-biennial oscillation (QBO) have been well documented in the subtropics and extratropics, for example for the stratospheric polar vortex (Holton and Tan, 1980; Anstey and Shepherd, 2014; Lu et al., 2020), the subtropical jets (Garfinkel and Hartmann, 2011; Hansen et al., 2016; Ma et al., 2021) and the North Atlantic Oscillation (Hansen et al., 2016; Gray et al., 2018; Andrews et al., 2019b). Observational and modelling evidence suggests that there is also a tropical route of influence of the QBO through impacts on monsoons (Giorgetta et al., 1999; Claud and Terray, 2007; Liess and Geller, 2012), the Intertropical Convergence Zone (ITCZ) (Gray et al., 2018), tropical sea-surface temperatures (SSTs) (Garfinkel and Hartmann, 2011; Huang

et al., 2012), tropical cyclones (Ho et al., 2009; Jaramillo et al., 2021) and most prominently, the MJO (Son et al., 2017; Lee and Klingaman, 2018; Wang et al., 2019; Martin et al., 2021b).

The tropical route of QBO teleconnections remains less well understood than other routes for various reasons, see Haynes et al. (2021) and Hitchman et al. (2021) for recent reviews on stratosphere-troposphere coupling in the tropics. The short observational record limits the confidence in any analysis that seeks to investigate differences between the two QBO phases in a 30-40-yr long dataset, as variability in the tropics on QBO time-scales is dominated by ENSO (Liess and Geller, 2012; Seo et al., 2013; Gray et al., 2018). Similarly, the modulation of the location and magnitude of convection in the tropical Pacific by ENSO events can influence the characteristics of the QBO (Taguchi, 2010; Schirber, 2015; Christiansen et al., 2016; Serva et al., 2020), which makes it difficult to separate the cause and effects of ENSO and the QBO.

The observational evidence available has shown surface impacts associated with the QBO over monsoon and oceanic regions in satellite-derived fields such as cloud height, occurrence and OLR (Collimore et al., 2003; Liess and Geller, 2012), as well as in surface precipitation diagnosed from gridded datasets or from reanalysis (Seo et al., 2013; Gray et al., 2018). This observational evidence shows zonally asymmetric impacts, indicative that the impact of the QBO is not consistent across all the equatorial latitudes but rather depends on longitude, which has been suggested (e.g. by Collimore et al., 2003; Liess and Geller, 2012) to be due to a QBO modulation of the Walker circulation, which has been shown in some reanalysis (Hitchman et al., 2021).

There is relatively less evidence from modelling studies, for e.g., Giorgetta et al. (1999) found that boreal summer monsoon regions exhibit a significant response in cloudiness to the QBO winds in a GCM. Nie and Sobel (2015) found that the influence of the QBO may depend on the strength of convection and SST forcing in a cloud-resolving model, suggesting a non-linear effect of the QBO over a convective profile. Only a relatively small number of studies have analysed tropical QBO teleconnections in CMIP5/CMIP6 models (Serva et al., submitted), as most CMIP analyses focus on the overall representation of the QBO and teleconnections to the extra-tropics (Richter et al., 2020; Anstey et al., 2021).

The physical mechanisms through which the QBO could influence tropical surface climate are also not well understood (see section 2.5.2). The influence of the QBO over the

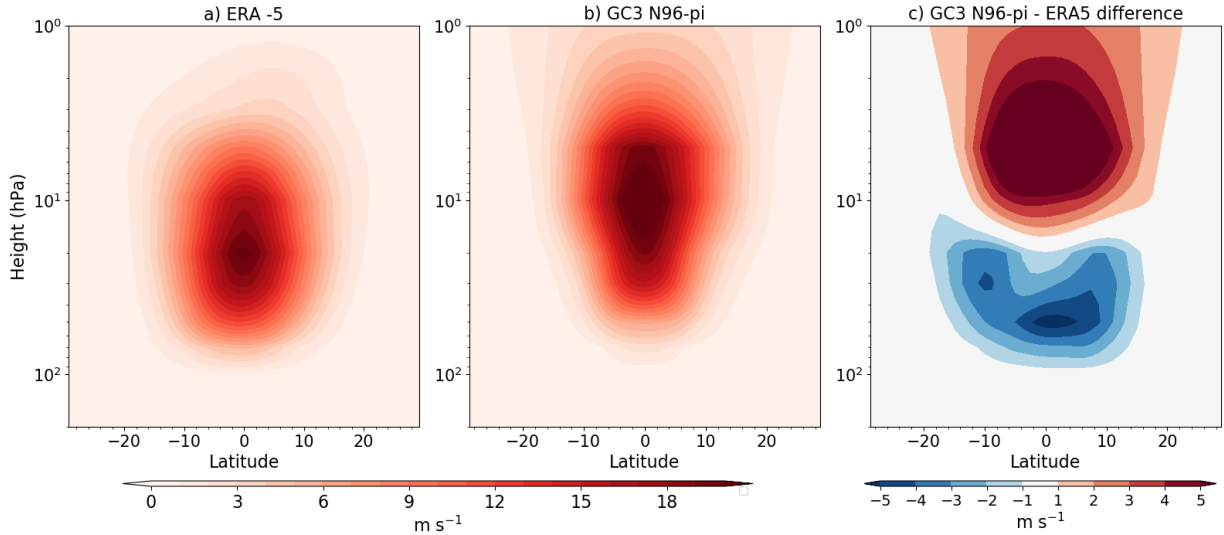


Figure 7.1: Latitude-pressure plot of the amplitude [m s^{-1}] of the QBO for (a) ERA5 and (b) GC3 N96-pi. (c) The difference in amplitude between the (b) model and reanalysis. Obtained from the zonal mean zonal wind fourier spectrum magnitude within the QBO periods, as in Schenzinger et al. (2017).

temperature and vertical wind shear near the tropopause layer (Tegtmeier et al., 2020b; Martin et al., 2021c) has been hypothesized to affect convection through several mechanisms. Early studies (Gray, 1984; Collimore et al., 2003) suggest that changes to the vertical wind shear or static stability in the upper-troposphere lower-stratosphere (UTLS) region induced by the QBO modify the depth of convection at equatorial latitudes. However, other studies suggest that the surface impact of the QBO may be a function of both the UTLS temperature changes and the tropospheric convective forcing (Nie and Sobel, 2015).

The leading hypothesis to explain an impact from the QBO on tropical deep convection suggests that changes to the UTLS static stability, caused by the QBO residual circulation, modifies the strength of convection (Collimore et al., 2003; Liess and Geller, 2012; Nie and Sobel, 2015). However, most of the existing climate models underestimate the amplitude of the QBO in the lowermost stratosphere (Figure 7.1) and by consequence the variability of the UTLS static stability associated with the QBO is lower in state-of-the-art GCMs (Schenzinger et al., 2017; Richter et al., 2020; Bushell et al., 2020). For example, the observed relationships between the QBO and the MJO have not been found in GCMs (Lee and Klingaman, 2018; Kim et al., 2020) and one reason for these results may be the underestimation of the UTLS

temperature variability associated with the QBO in current GCMs.

In addition, only a relatively small number of studies have analysed tropical QBO teleconnections in a GCM, specifically in CMIP5/CMIP6 models (Serva et al., submitted), as most CMIP analyses focus on the polar and subtropical routes of QBO influence (Richter et al., 2020; Anstey et al., 2021). Biases in the stratosphere of GCMs such as the weaker amplitude of the QBO in the lower stratosphere have led several studies to perform experiments in which the model stratosphere is relaxed towards an observed or idealized state, more commonly known as nudging (e.g. Garfinkel and Hartmann, 2011; Lee and Klingaman, 2018; Gray et al., 2020; Richter et al., 2020; Martin et al., 2021a). The nudging technique has proven useful because the relaxation can remove biases, identify causal pathways and test specific hypotheses regarding the mechanisms (Gray et al., 2020; Martin et al., 2021a; Haynes et al., 2021).

In short, there is a lack of robust evidence for QBO surface impacts in the tropics as QBO-related anomalies in observations may be the result of chance or the upward effect of tropical convection on the characteristics of the QBO. Moreover, there is little modelling evidence of QBO impacts in the tropics, particularly with state-of-the-art GCMs. The Met Office Hadley Centre (MOHC) Unified Model (UM) exhibits an internally generated QBO that is reasonably similar to observations, except for the weak amplitude bias in the lower stratosphere (Richter et al., 2020). Moreover, nudging has been successfully applied to this model in previous studies (Telford et al., 2008; Gray et al., 2020). For these reasons, the UM is ideal to investigate whether there are any surface impacts in the tropics associated with the QBO and what mechanisms may be at play in the observed stratospheric-tropospheric coupling.

This chapter first investigates QBO tropical teleconnections in the pre-industrial control simulations of the MOHC from CMIP6. This first part of the chapter examines whether there are any robust relationships between surface precipitation and the QBO. We then systematically explore evidence for a QBO impact on the major modelled tropical climate circulations, taking advantage of the extremely long simulations that can provide improved estimates of statistical significance when compared with the relatively short observational and reanalysis datasets.

The first part will demonstrate robust links between the QBO and several features of tropical climate but no conclusive statement can be made on the direction of causality using these datasets. For that reason, nudging experiments feature in the second part of the chapter. Atmosphere-only and coupled model simulations are analysed to evaluate the effect of improving the biases of the QBO amplitude on the surface response. Specifically, these experiments test the UTLS static stability hypothesis, so that stronger effects would be expected in a model with a stronger UTLS temperature variability associated with the QBO compared to a model with a weaker UTLS static stability effect of the QBO.

The methodology and data used in this chapter are presented first in section 7.2, including the details on the nudging experimental setup. Then, the QBO impacts in the CMIP6 experiments are diagnosed and described in section 7.3. Section 7.4 examines the results from the nudging experiments. A discussion and conclusions are presented at the end of the chapter.

7.2 Methods and data

The observational datasets and reanalysis (ERA5) used in this chapter are described in more detail in section 3.1 and consist of the HadSST3 dataset for SST, GPCP for precipitation and ERA5 for the rest of the diagnostics that include the zonal and meridional winds, air temperature, etc.

7.2.1 CMIP6 data

In section 7.3, three pi-control experiments are analysed: HadGEM3 GC3.1 at N96 and N216 horizontal resolutions (hereafter referred to as GC3 N96-pi and GC3 N216-pi) and UKESM at N96 horizontal resolution (hereafter referred to as UKESM N96-pi). The N96 and N216 atmospheric resolution is $1.875^\circ \times 1.25^\circ$ and $0.83^\circ \times 0.56^\circ$, respectively whereas the oceanic resolutions are 1° (ORCA1) and 0.25° (ORCA025), respectively. The full 500 years available of the GC3 N216-pi simulation are used and although more data exists for UKESM-pi and GC3 N96-pi, we use 500-yrs of these simulations as well for consistency. The three simulations chosen use the same model setup, with constant year 1850 forcing,

but differ in their horizontal resolution or the treatment of aerosol-chemistry processes and land-surface interactions (see section 3.2). The CMIP6 version of the model extends to the lower mesosphere and includes a self-generated QBO via a non-orographic gravity wave scheme that compares well with the observed QBO (Richter et al., 2020).

Pre-industrial control experiments are fit for the purpose of examining the internal variability of a model and mechanisms because external forcing is kept constant throughout the usually long integrations (e.g. in CMIP6 these experiments are at least 500 years long). For this reasons, multiple studies have used this type of experiments to investigate teleconnections and variability on multiple time-scales and for many different purposes (see e.g. Watanabe et al., 2012; Zanchettin et al., 2014; Palmer and McNeall, 2014; Menary et al., 2018; Dimdore-Miles et al., 2021; Villamayor et al., 2021). For the purposes of this chapter, the QBO effect can be examined in the model as various cycles of decadal variability are sampled throughout the 500 yr of the integration. Note that the variability of the pre-industrial control experiments is compared against the variability of observations with the caveat the greenhouse forcing may play a role for the observed responses.

The majority of the diagnostics in section 7.3 are shown for the higher resolution GC3 N216-pi simulation and comparisons with the other two simulations are noted where appropriate. The equatorial climate of GC3 N216-pi captures tropical dynamical processes and tropical mean and extreme precipitation reasonably well relative to lower-resolution configurations (García-Franco et al., 2020; Abdelmoaty et al., 2021). This configuration has been top ranked amongst all CMIP5/CMIP6 models in metrics such as the seasonal-phase locking and amplitude of ENSO (Menary et al., 2018; Richter and Tokinaga, 2020; Liu et al., 2021), extreme precipitation (Abdelmoaty et al., 2021) and the annual cycle of equatorial Atlantic SSTs and low-level winds (Richter and Tokinaga, 2020). The HadGEM model has also been historically top ranked in the representing the stratosphere and the QBO (Schenzinger et al., 2017; Richter et al., 2020). However, several biases are notable in this model, particularly in tropospheric dynamical features such as the southward bias of the Atlantic ITCZ linked to the dry Amazon bias and too strong precipitation rates over the East Pacific ITCZ (García-Franco et al., 2020).

7.2.2 Indices

For the QBO, the monthly-mean equatorially averaged [5°S-5°N] zonal mean zonal wind at 70 hPa is used and each phase of the QBO is defined using the threshold of 2 m s⁻¹ (Garfinkel and Hartmann, 2010), so the westerly phase (QBOW) is defined for months with an index value above 2 m s⁻¹ and the easterly phase (QBOE) for index values below -2 m s⁻¹. For ENSO, the EN3.4 SST index is used, with a running-mean of 5 months and a threshold of ±0.5 K used to define positive or negative events. Neutral months are defined where the running-mean of EN3.4 index is smaller than ±0.5 K.

The amplitude and descent rates of the QBO are calculated using the deseasonalized zonal mean equatorially averaged in equatorial latitudes for all levels. The amplitude (A) of the QBO is defined using the first and second principal components (PCs) empirical orthogonal function (EOF) decomposition of the 10-70 hPa wind time-series (Serva et al., 2020) as $A = \sqrt{PC1^2 + PC2^2}$. The descent rates are calculated following Schenzinger et al. (2017) for descending westerly and easterly phases individually by finding the level of the zero wind line ($u = 0$) for each month and computing the difference between consecutive months. These definitions of the amplitude and descent rates were chosen to evaluate the influence of ENSO on the whole profile of the QBO and not just one single level.

An index for the Indian Ocean Dipole (IOD) was also required and this chapter uses a convective precipitation index of the zonal gradient in the Indian Ocean (convective IOD Index), defined as the difference of the deseasonalized area-averaged convective precipitation between the western [50-70°E] and eastern [80-100°E] equatorial [10°S-10°N] Indian Ocean, which is in a similar region as the standard SST IOD index (Wang and Wang, 2014). This convective precipitation is used to define IOD events with a 1 standard deviation threshold to define positive and negative events.

7.2.3 Analysis techniques

Composite analysis is the primary technique used in the study. For each month the QBO phase (QBO-E or QBO-W) and the ENSO phase (El Niño, La Niña or neutral ENSO phase) was determined as described above. Annual-mean and seasonal-mean composites

were derived by computing weighted averages to account for differences in the counts of each month. This means the composites were derived by weighting each monthly-mean by its size and then computing the seasonal or annual-mean average so that all months contribute equally and there is no seasonal effect due to, e.g., QBO or ENSO phase-locking.

The length of the pre-industrial control experiments is such that the number of total El Niño and La Niña months for GC3 N216-pi were over 1000 months in the entire simulation for each phase, and over 1500 months for each QBO phase. Moreover, El Niño months found under QBOW were 376 and 284 under QBOE, whereas in the observed 1979-2018 period, 62 QBOW El Niño months and 36 QBOW El Niño months were diagnosed.

Linear regression analysis has proven useful to understand the effect of one or more aspects of the climate over a region or a time-series, and was used to investigate the surface impacts of the QBO in observations by Gray et al. (2018). A simple linear regression model can be written as:

$$Y(t) = X_0 + X_i(t)\beta_i + \epsilon, \quad (7.1)$$

where Y is the measured or dependent variable, X_0 is a constant coefficient, β_i is the regression coefficient between X_i and Y and ϵ represents random error or a residual. In all cases, the models solved using an ordinary least-squares (OLS) method. A multivariate regression model can be used to study the joint effect of two or more predictors over a variable (Y) such that the model can be written as:

$$Y(t) = X_0 + \sum_j^N X_j(t)\beta_j + \epsilon \quad (7.2)$$

where $X_j(t)$ is any predictor with an associated regression coefficient β_j . As in previous studies (Gray et al., 2018; Misios et al., 2019), the regression coefficient can be rescaled to evaluate the total effect that a predictor (X_j) can have on the variance of the measured variable (Y) using the standard deviation (σ_j) and the maximum ($X_{j,max}$) and minimum ($X_{j,min}$) values of X_j so that the rescaled coefficient β'_j can be written as:

$$\beta'_j = \beta_j \frac{X_{j,max} - X_{j,min}}{\sigma_j}. \quad (7.3)$$

7.2.4 Nudging experimental setup

This section describes the experimental setup for the nudging experiments. The GC3.1 configuration of the UM model is used (model version 11.4), using an atmospheric horizontal resolution of N96 (corresponding to the low-resolution version of the MOHC CMIP6 simulations). Both atmosphere-only and ocean-atmosphere coupled experiments were conducted for the period 1981-2015, using a present-day climate setup where all external forcings, including greenhouse gas and aerosol emissions, are set constant to those of the year 2000.

Nudging refers to the relaxation of a model variable towards a specified state which can be from reanalysis, observations or idealized states (Gray et al., 2020; Martin et al., 2021a). In the UM setup, three variables can be relaxed, air temperature (T) and the zonal (u) and meridional (v) components of the wind. The relaxation is applied at each grid-point, in contrast to the setup in other models (e.g. Martin et al., 2021a) where the relaxation is performed in a zonal-mean sense. Specifically, the UM uses a Newtonian relaxation technique (Telford et al., 2008; Gray et al., 2020) which sets the field to be relaxed (F) at each time-step through the following equation:

$$\Delta F = G\Delta t(F_{ndg} - F_{model}), \quad (7.4)$$

where ΔF is the discrete change of F at each time-step, G is the relaxation parameter, Δt is the time-step size, F_{ndg} is the value of the field from the nudging data and F_{model} is the model value of the field at the last time-step (Telford et al., 2008).

The relaxation parameter G sets the strength of the relaxation and is linked with the relaxation timescale (τ) by $G = 1/\tau$. In the UM model, the relaxation timescale is given by the temporal resolution of the nudging data, which is 6-h (Telford et al., 2008; Gray et al., 2020), so that $G = \frac{1}{6} \text{ h}^{-1}$. This relaxation parameter has been shown to be sufficiently strong to constraint the stratospheric state of the model (Gray et al., 2020) and so the same parameter was used for the simulations of this chapter.

Furthermore, the nudging can be performed between specified vertical levels and in selected latitude/longitude regions with *tapering*. The tapering refers to a linear interpolation

Table 7.1: Experimental setup indicating the model configuration, the period, ensemble members (Ens.) acronym and relaxation details.

Setup	Period	Ens.	Name	Nudging
Atmosphere-only	1981-2015	3	AMIP	ERA5. U-only 90 hPa
Atmosphere-only	1981-2015	2	AMIP-Control	No
Atmosphere-only	1981-2015	3	AMIP-Shifted	ERA5. U-only, 90 hPa. Relaxation shifted -1 year.
Coupled	1981-2015	6	Coupled Nudged	ERA5. U-only 90 hPa.
Coupled	1981-2015	2	Coupled Control	No.

between the maximum G and zero nudging ($G = 0$). For example, a tapering of 4 vertical levels was applied in our simulations which means that there was a linearly increasing G from a bottom level with no nudging to the level where the specified G is implemented; the same linear interpolation works for latitudinal tapering.

The experimental design chosen relaxes the zonal wind (u) in the model levels corresponding to 90 hPa to 4 hPa, with a tapering of 4 levels, which means that full nudging was only working from 70 hPa to 10 hPa. The nudging was done at all longitudes in the latitude band of 10°S-10°N with a latitudinal tapering of 10 degrees on both sides, which means that at 20°N the relaxation parameter was 0. The experimental setup aims to reasonably simulate the observed variability of the zonal wind leaving the meridional component of the wind and the temperature to respond freely within the model.

Atmosphere-only and coupled ocean-atmosphere simulations were performed with this nudging setup, with corresponding control simulations in which there was no relaxation of any kind (Table 7.1). The atmosphere-only (AMIP) experiments were run with observed SSTs using the CMIP6 SST dataset used for AMIP experiments, note the surface boundary SSTs are used at all latitudes. The coupled experiments use an oceanic resolution of 0.25° (ORCA025) using the NEMO model (Storkey et al., 2018). Each ensemble member was initialized from different ocean/atmosphere initial conditions in order to decrease the role that internal variability may have on these simulations. For each of the configurations several ensemble members were launched (see Table 7.1).

Note that the coupled experiments differ only slightly from the setup used in the CMIP6 piControl experiments, with the atmospheric resolution matching the resolution of GC3

N96-pi ($1.875^\circ \times 1.25^\circ$) and the oceanic resolution being the same as GC3 N216-pi (0.25°). The forcing is constant in both types of runs, except that in the piControl experiments, the forcing represents conditions of the year 1850 and in these experiments the forcing is for the year 2000.

In addition to the nudged and control coupled and AMIP experiments, we performed another type of atmosphere-only experiment. In the normal AMIP Nudged experiment, the SST driving data corresponds to the same year as the imposed zonal wind in the equatorial stratosphere that was observed in the real-world. To explore possible feedback processes between QBO winds and the SSTs, we performed an AMIP Shifted experiment, where the nudging data was shifted with a -1 year lag from the SSTs. In this experiment, e.g., the model year 1997 was run using 1997 SSTs but zonal winds in the stratosphere corresponding to 1996 of ERA5. In this way we have minimised any in-phase relationship between the QBO phase and the SSTs. An alternative approach would be to *shuffle* the SSTs so that each year is run with randomly selected SSTs. However, since we are performing multi-year simulations shuffling has associated issues of how to join the randomly-selected SSTs at the year-boundary to form a coherent multi-year SST time-series. To avoid this issue we decided to simply shift the SSTs by one year so the QBO phase and SSTs were not aligned.

7.3 Teleconnections in the pre-industrial control experiments

The tropical precipitation response to the QBO phase is analysed in both observations and model simulations, first in the annual-mean and then by season(section 7.3.1). The potential for aliasing with the ENSO signal is investigated (section 7.3.2) and QBO-ENSO interactions are further explored (section 7.3.3), as well as QBO interactions with the Indian Ocean dipole (IOD). Finally, interactions between the QBO and the Indian Ocean, the ITCZ, monsoons and the Walker circulation are identified and discussed in 7.3.4.

7.3.1 Precipitation

QBO composite differences in annual mean precipitation (QBO-W minus QBO-E) are shown in Figure 7.2 from the gridded GPCP observational dataset and from all three model

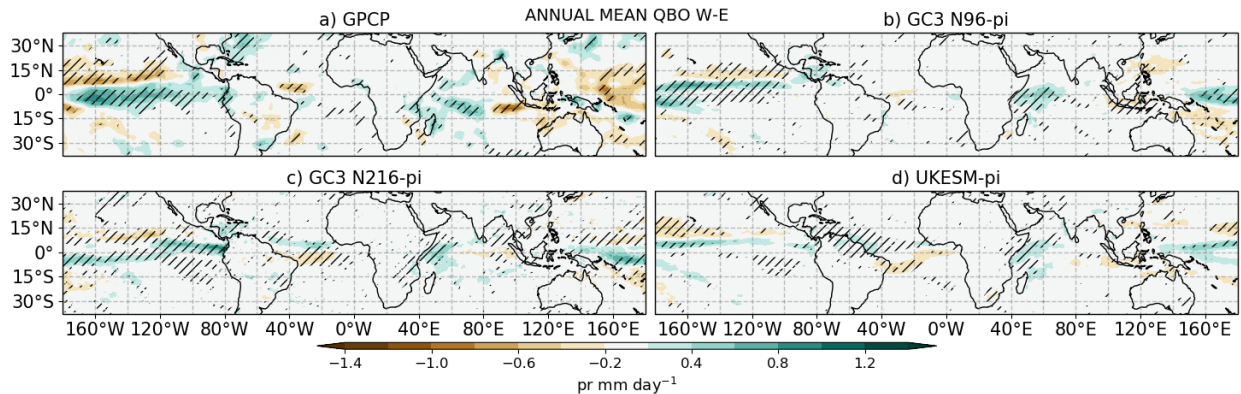


Figure 7.2: QBO-W minus QBO-E composite differences in annual-mean precipitation from (a) GPCP, (b) GC3 N96-pi, (c) GC3 N216-pi and (d) UKESM-pi. Hatching denotes statistically significant differences at the 95% confidence level using a bootstrapping with replacement test.

simulations. In the observations the QBO signals are largest and statistically significant in the tropical Pacific, equatorial Atlantic and Indian Oceans, in good agreement with previous analyses (Liess and Geller, 2012; Gray et al., 2018). The three simulations agree reasonably well with the GPCP distributions and amplitudes, particularly in the Pacific and Indian Oceans. Positive differences of up to 1.2 mm day^{-1} are found in the equatorial Central Pacific and the Indian Ocean and negative differences of up to 0.6 mm day^{-1} in the off-equatorial North Pacific, although the differences are smaller in the simulations than observed.

In the tropical Atlantic, however, there is an indication of a weak but significant signal in the observations near the ITCZ but the models show a signal of the opposite sign in this region (or the absence of a signal in the case of GC3 N96-pi). This disagreement with observations may be due to the biased southward position of the Atlantic ITCZ in the model which is more pronounced in DJF (García-Franco et al., 2020).

The QBO signal in precipitation is found to be strongly dependent on the seasonal cycle in both models and observations. Figure 7.3 shows a comparison of the GPCP dataset and GC3 N216-pi for individual seasons (see Figure S1 for corresponding fields from the other models). The positive equatorial Pacific signal in the GPCP dataset, which resembles an El Niño anomaly, is particularly strong and statistically significant in December-January-February (DJF) (Fig. 7.3a). A similar pattern is present in both March-April-May (MAM) (Figure 7.3c) but with no statistical significance. In GC3 N216-pi the QBO signal in the

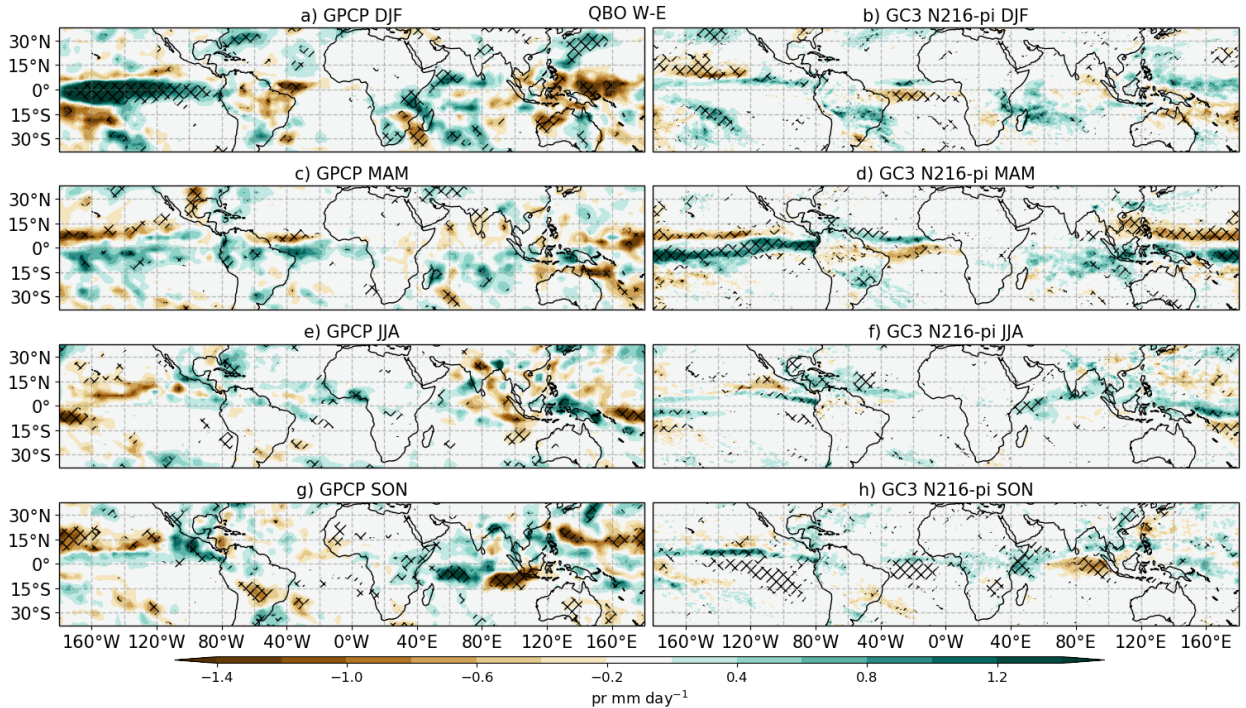


Figure 7.3: As in Figure 7.2, but showing seasonal-mean QBO composite from (left) GPCP and (right) GC3 N216-pi for DJF, MAM, JJA and SON from top to bottom.

Pacific is significant in all seasons, likely due to the greater number of years in the ensembles, although it is shifted slightly compared to GPCP and is strongest in MAM (Fig. 7.3c).

In the Atlantic, the QBO signal in the ITCZ region is more clearly evident in the individual seasons. In DJF there is reasonable similarity between the model and observations but by MAM the opposite sign of the model compared to GPCP becomes evident, even though the ITCZ bias in the model is stronger in DJF than in MAM (García-Franco et al., 2020). In addition, all models and GPCP indicate that the Caribbean Sea is wetter in JJA during QBO-W than in QBO-E (see Figs. 7.3 and S1). In the Indian Ocean, the observations and all models show relatively large and significant differences in SON, (Fig. 7.3e-f), characterized by a dipole of wet anomalies to the west and dry anomalies to the east. The dipole anomalies suggest a possible QBO influence on the IOD, which is characterized by a zonal gradient of SSTs and convective activity in the Indian Ocean that is specially prominent in SON (Saji et al., 1999; Deser et al., 2010; McKenna et al., 2020). This possibility is explored further in section 7.3.3 below.

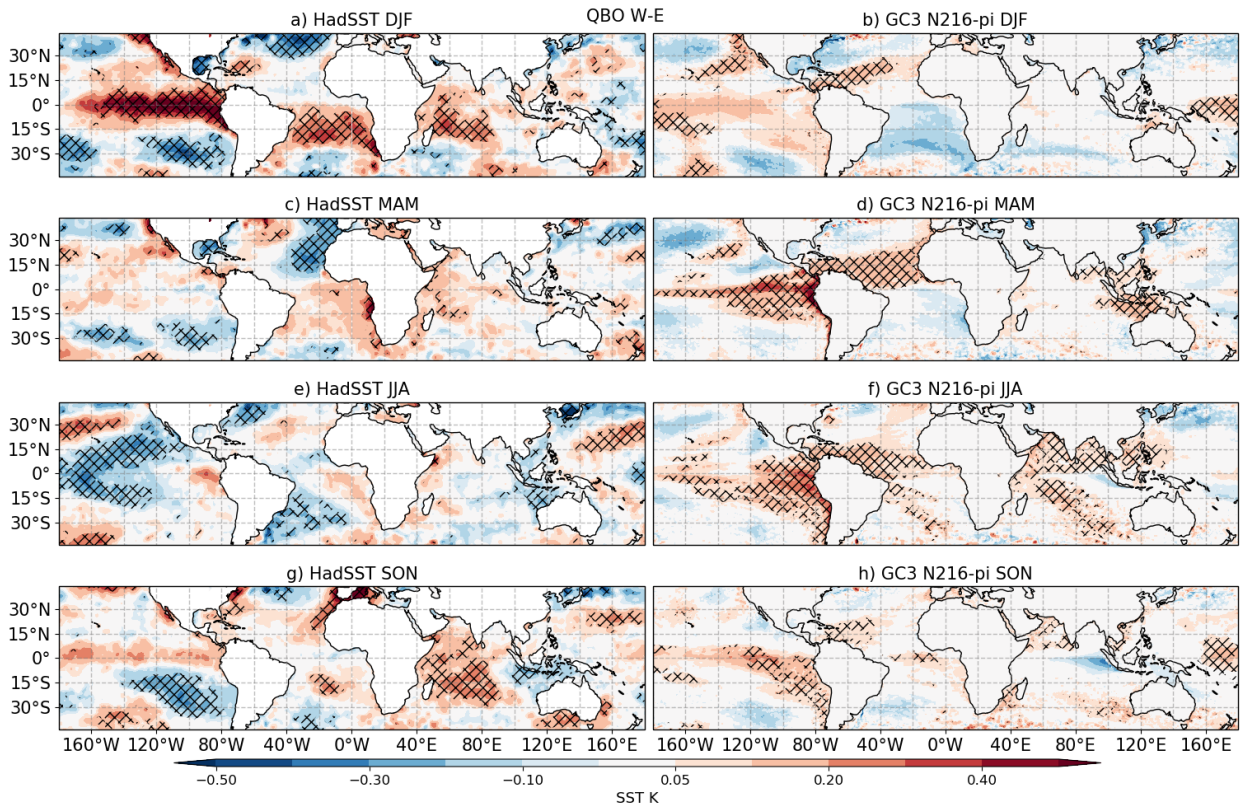


Figure 7.4: As in Figure 7.3 but for seasonal-mean sea surface temperatures from (left) the HadSST dataset and (right) GC3 N216-pi simulation.

In summary, the GPCP total precipitation composite analyses are consistent with previous analyses (Liess and Geller, 2012; Gray et al., 2018). These composites show a zonally asymmetric QBO signal primarily over the oceans in which the modelled QBO response patterns are in good agreement with the GPCP analysis. This good agreement, together with the extended duration of the model simulations (500 years) compared with the available observations, suggests that analysis of the modelled QBO signals may help to understand the mechanisms that give rise to the surface response in the QBO. However, the QBO signals from both model and observational analyses show strong similarities to well-known response patterns for ENSO and the IOD. Previous observational studies have also shown a higher frequency of El Niño events during QBOW and of La Niña during QBOE in observations since 1979 (Taguchi, 2010; Liess and Geller, 2012), although the observational record is short so there is much statistical uncertainty. Therefore, there is potential for aliasing of the signals, which needs further investigation.

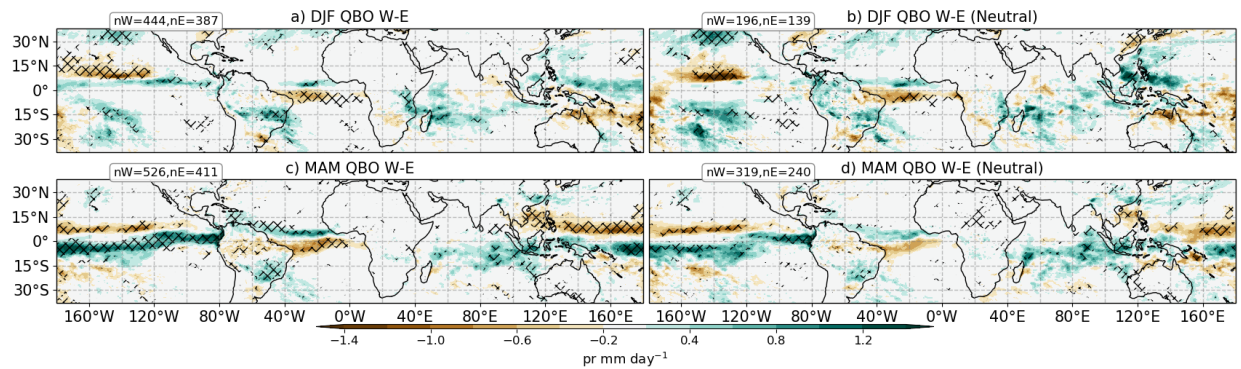


Figure 7.5: Composite QBO W-E differences of total precipitation in GC3 N216-pi in (a, b) DJF and (c, d) MAM for (a, c) all the events and (b, d) Neutral ENSO conditions only. The sample size of each composite is noted in the top left corner of each panel. Statistically significant differences to the 99% confidence level are shown through the hatching.

7.3.2 Potential aliasing of QBO and ENSO signals

To further explore the QBO signal and its interaction with ENSO, Figure 7.4 shows the QBO signal in SSTs. The QBOW minus QBOE composite differences are shown for individual seasons from the HadSST dataset and the GC3 N216-pi model simulation. The SST signals are consistent with the precipitation signals. Both model and observational datasets show significant positive SST responses in the equatorial Pacific that are similar to El Niño patterns. In the HadSST dataset the Pacific response is strongest in DJF and resembles an East Pacific (or ‘standard’) El Niño, whereas the simulated anomalies in DJF (for all models, see Fig. S2) are weaker and look more like a central Pacific El Niño (Capotondi et al., 2015).

In GC3 N216-pi, the largest differences are observed in MAM in the easternmost Pacific Ocean and thus more closely resembles the observed DJF response pattern. In the South Atlantic the model shows a region weak, insignificant cooling in DJF (Figure 7.4d), in contrast to the statistical significant warming signal in HadSST (Figures 7.4a,c). In the northern tropical Atlantic the model shows a year-long warming signal with stronger anomalies in MAM and JJA; this signal is present in HadSST but only found in JJA and SON and it is not significant (Fig. 7.4e, g). The simulated northern tropical Atlantic warm anomalies in DJF (Figure 7.4b) are accompanied by a warmer Caribbean Sea and a cooling of the Gulf of Mexico, warmer SSTs along the coast of California and a cooling of the central North Pacific, all of which resemble the impact of El Niño events and the

positive phase of the Pacific North American (PNA) pattern (Deser et al., 2010; Guo et al., 2017; Jiménez-Esteve and Domeisen, 2020).

As an initial investigation of the possibility of aliasing between the QBO and ENSO signals, Figures 7.5a,b shows the DJF QBOW minus QBOE composite differences of total precipitation from the GC3 N216-pi simulation using all years (as in figure 7.3) compared with using only those years identified as ‘ENSO-neutral’. Although the sample size is substantially reduced in the latter (see figure for the number of months in each QBO composite) the sample size is nevertheless still large (>120 data points in each composite). The response patterns are similar in each plot, which suggests that the QBO signal is unlikely to be the result of a sampling bias that favours one particular phase of ENSO.

An alternative approach to investigate the possibility of aliasing of the QBO/ENSO signals is to use a multi-linear regression technique (see section 2) in which the signal is analysed for both QBO and ENSO simultaneously. Here, we switch to analysing convective precipitation to better investigate the possible influence of the QBO on deep tropical convection.

Figures 7.6a,b show results from a simple linear regression analysis of the monthly-averaged time-series of GC3 N216-pi total precipitation in which a single QBO index is employed. Figure 7.6a includes all available years while Figure 7.6b includes only neutral ENSO years. The results are very similar to the annual-mean composite differences in total precipitation (7.2), with increased convective precipitation over the equatorial Pacific when the zonal winds at 70 hPa are positive.

Figures 7.6c,d show the ENSO and QBO signals when the Nino3.4 index is included as well as the QBO index. The ENSO response is clearly evident, highly statistically significant and compares well with the well-known patterns obtained from observations. The amplitude of the ENSO signal is also much larger than the QBO signal. Nevertheless, the QBO signal remains intact and all of the main features are still significant (Fig. 7.6c). For example, the positive regression coefficients that suggest a northward shift of the Atlantic ITCZ and the wetter Caribbean Sea and western Indian Ocean in the simple regression model are still found in the multivariate regression analysis.

These results suggest that the modelled QBO signal in total precipitation does not arise due to a simple aliasing of the signal with ENSO. However, the multi-linear regression

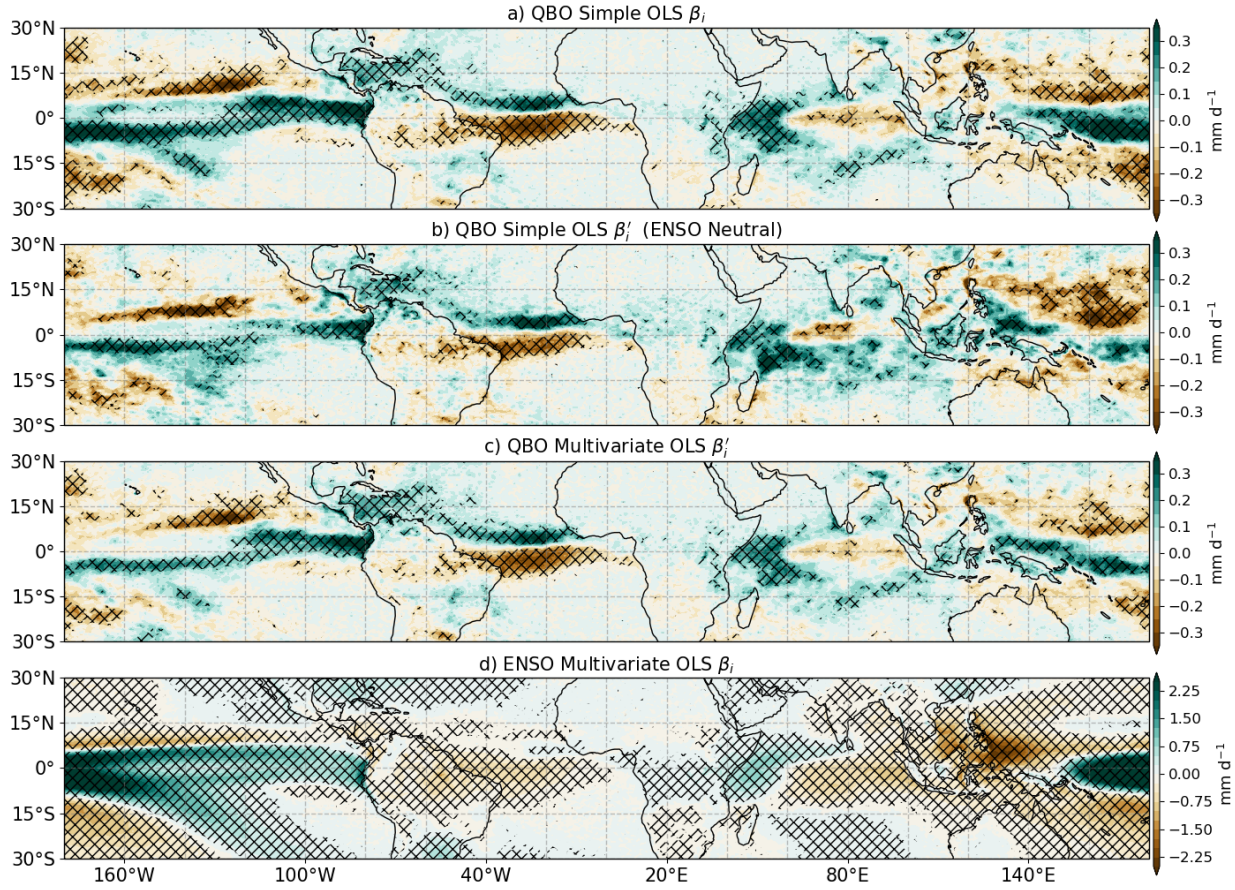


Figure 7.6: Annual-mean regression model results in GC3 N216-pi for convective precipitation. (a, b) Regression coefficients (β_i) from a simple ordinary least-squares (OLS) regression model with the QBO index for (a) all months and (b) ENSO-Neutral months only. (c, d) show the regression coefficients resulting from a multivariate regression model using the ENSO and QBO indices for the (c) QBO and (d) predictors. In all cases, the regression coefficients are rescaled by multiplying the regression coefficients with the ratio of maximum amplitude and standard deviation of the QBO or ENSO indices.

technique assumes that the QBO and ENSO indices are orthogonal and that their responses add together linearly. The similarity of the two responses indicate that this is clearly not the case and there is substantial interaction between the two phenomena. Nevertheless, the QBO signal remains even when only neutral-ENSO years are included in the analysis, suggesting that the QBO has a real influence on the surface precipitation.

7.3.3 Interaction of the QBO with ENSO and IOD

To further explore the interaction of the QBO and ENSO, we first investigate whether aspects of the QBO are influenced by ENSO events. This relationship could be a real possibility since

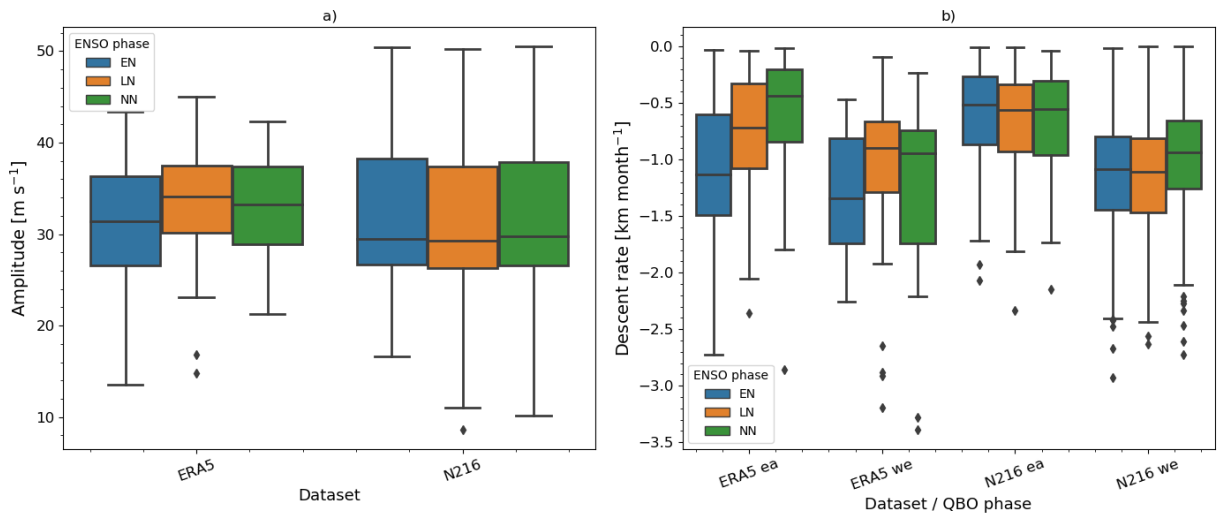


Figure 7.7: Box plots of QBO (a) amplitude [m s^{-1}] and (b) descent rate [km month^{-1}] separated by dataset (ERA5 and GC3 N216-pi) and ENSO phase. NN stands for Neutral ENSO. In (b) descent rates are shown for both descending easterly (ea) and westerly (we) phases following Schenzinger et al. (2017).

the intrinsic mechanism of the QBO involves tropical waves that are generated within the troposphere. Schirber (2015) found in a GCM that under El Niño conditions tropospheric wave activity increases and accelerates the downward propagation speed of the QBO westerly phase. However, the analysis by Serva et al. (2020) shows that only models with high resolution can reproduce the observed ENSO effects on the QBO amplitude while several models show no impact of ENSO on the QBO.

For that reason, we analyse several characteristics of the QBO and their dependence on ENSO phase, namely the descent rate and the amplitude of the QBO (see the 'Methods and Data' section for details of how the QBO amplitude is defined). The results are summarised in Figure 7.7 for the ERA5 reanalysis dataset (35 years; 1979 – 2014) and for the GC3 N216-pi simulation (500 years). In ERA5, the well-known faster descent rates during the westerly phase than in the easterly phase is clearly evident and agrees well with studies of longer datasets such as the Berlin radiosonde data (Schenzinger et al., 2017). Also, the ERA5 QBO descent rates and the amplitude both depend on the phase of ENSO. A higher amplitude and slower descent rates are observed during La Niña phases and weaker amplitudes and faster descent rates during El Niño.

Table 7.2: ENSO and IOD events frequency (month month⁻¹). For positive and negative events, for each mean value the error shown is the standard deviation of the probability density distribution (PDF) found by bootstrapping with replacement. Results in **bold** indicate that the event frequency PDF for QBOW is significantly different to QBOE to the 95% confidence level according to the KS test.

Dataset	QBO phase	El Niño	La Niña	IOD+	IOD-
GC3 N216-pi	W	0.24±0.09	0.19±0.05	0.17±0.03	0.11±0.02
GC3 N216-pi	E	0.21±0.07	0.26±0.07	0.12±0.03	0.15±0.03
ERA5/HadSST	W	0.28±0.01	0.27±0.02	0.17±0.01	0.13±0.01
ERA5/HadSST	E	0.17±0.02	0.27±0.03	0.12±0.01	0.19±0.03

In the model, the descent rates are also faster for the westerly than the easterly QBO phase, as observed, but the relationship between the QBO characteristics and ENSO is less clear. Neither the amplitudes nor descent rates of the QBO are significantly different between El Niño (EN) and La Niña (LN) phases. Interestingly, the only significant difference in the model is that descending westerlies are slower in Neutral ENSO months compared to EN or LN conditions, perhaps suggesting that tropical wave activity is increased in both ENSO phases compared with neutral years. The model results therefore suggest that there is little influence of ENSO on the descent rate and amplitude of the QBO in the GC3 N216-pi simulation. This finding of a null influence of ENSO on the QBO agrees well with the results of Serva et al. (2020) that examined these relationships in an older version of the HadGEM model. In summary, there is no evidence to suggest an influence of ENSO on the QBO in the model.

The reversed possibility, that the QBO may somehow influence ENSO events is now examined. A higher frequency of EN events during QBOW and of LN during QBOE has previously been noted (Taguchi, 2010; Liess and Geller, 2012) although the short observational record means that there is statistical uncertainty. In Table 7.2 we document the frequency of ENSO events in each QBO phase from the ERA5 reanalysis dataset and from the GC3 N216-pi simulation. Probability density functions (PDFs) were constructed for the model data using 36-yr samples with replacement and a Kolmogorov–Smirnov

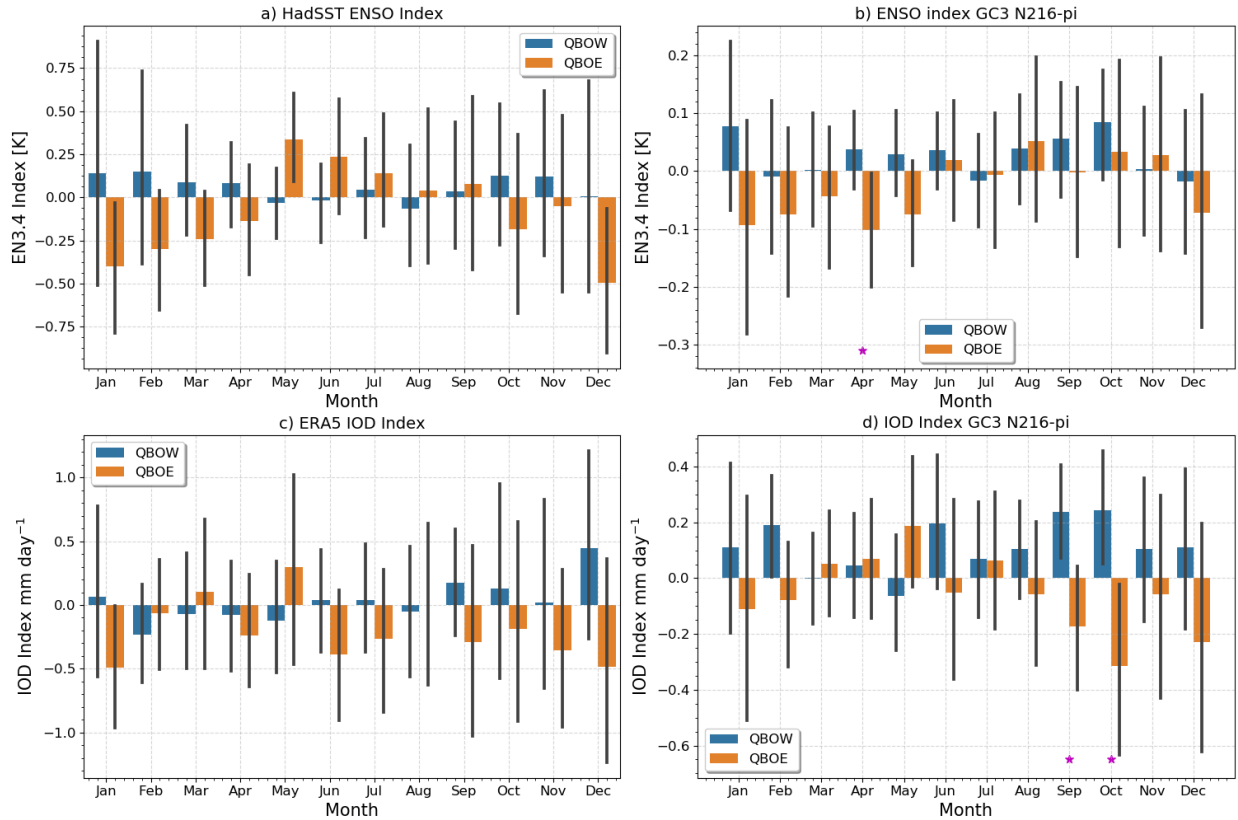


Figure 7.8: Monthly-mean (a-b) ENSO and (c-d) IOD-prc indices separated per QBO phase in (a, c) observations/reanalysis and (b, d) GC3 N216-pi. The error bars show the standard deviation of each index for each month and significant differences between QBO W and E months are highlighted with a * at the bottom of each panel.

(KS) test was used to evaluate if the PDFs of an event frequency (e.g. El Niño) were distinguishable for each phase of the QBO.

The results show significant differences for each ENSO phase in GC3 N216-pi (and this is also the case for the GC3 N96-pi and UKESM-pi simulations, not shown). El Niño events are more frequent under QBOW conditions than under QBOE in both observations and model datasets. La Niña events are equally frequent in both QBO phases in the HadSST dataset but in GC3 N216-pi they are more frequent under QBOE than under QBOW.

Figure 7.8a,b shows the EN3.4 index amplitude and interannual standard deviation as a function of each month from the HadSST dataset and the GC3 N216-pi simulation, separated for each phase of the QBO. From this we can examine, for example, whether any QBOW minus QBOE differences in ENSO characteristics arise primarily from one QBO phase or the other (i.e. a non-linear response) or whether both phases contribute

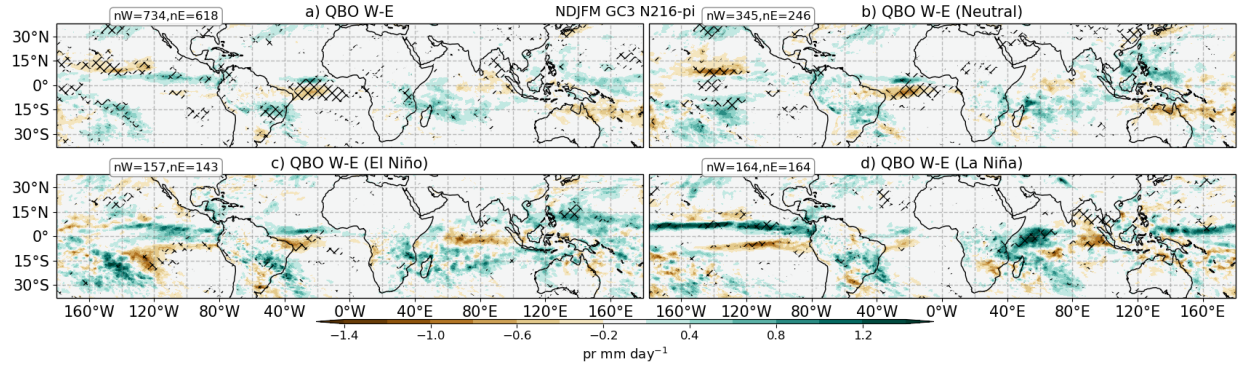


Figure 7.9: Composite QBO W-E precipitation differences of total precipitation in GC3 N216-pi in the peak ENSO season (NDJFM) for (a) all the events and (b) Neutral ENSO conditions only, (c) El Niño and (d) La Niña. The sample size of each composite is noted in the top left corner of each panel. Statistically significant differences to the 99% confidence level are shown through the hatching.

equally to the response difference. There are significant QBO differences in EN3.4 SST in both the HadSST and GC3 N216-pi datasets. In particular, the mean ENSO indices are very frequently positive in QBOW and negative in QBOE months from September until January. In the model, the differences are largest from Feb-to-May (in good agreement with the results shown in Figure 7.3).

Figure 7.8 also suggests substantial non-linearities in the QBO-ENSO interactions, since the amplitude of the EN3.4 anomaly in each month under QBO E/W conditions is seldom equal and opposite. This non-linearity is also evident in Figure 7.9 where the QBO composite differences in total precipitation during the peak ENSO season (November through to March) are shown using all years, only Neutral ENSO years and only EN or LN years. While the broad nature of the QBO signal remains similar, the details differ depending on the phase of ENSO (7.9c,d). For example, the Atlantic ITCZ response is most prominent in EN and Neutral years (Figure 7.9c) whereas the off-equatorial Pacific response is only found under Neutral years.

Positive differences in the western Indian Ocean and in the northern tropical Pacific are much stronger during LN (Fig. 7.9d) than in other ENSO phases. These results can be interpreted as EN and LN teleconnections being slightly different for each QBO phase. For example, in South America, more specifically in the South Atlantic Convergence Zone region (Jorgetti et al., 2014), wetter conditions during QBOW compared to QBOE are

found in all years and for both LN and EN conditions which indicates that in this model simulation, ENSO teleconnections to South America are also dependent on the QBO phase and the response in all years is the combination of ENSO phases.

Returning to Figure 7.8, during Dec-March in HadSST and Jan-May in GC3 N216-pi the QBO signal comes primarily from the QBOE phase, since the EN3.4 amplitudes are near zero under QBOW in these months. These results are consistent with the analysis of ENSO frequency in Table 7.2, which shows more frequent La Niña events under QBOE and El Niño events under QBOW. These results also suggest, therefore, that a stronger amplitude La Niña event in DJF may develop if there is a QBOE phase present in the lower stratosphere.

In the previous sections the precipitation and SST analyses also showed suggestive evidence of a relationship between the QBO and the IOD, in both the observations and the model. A link between the QBO and the IOD index and event frequency have been analysed in the same way as for the ENSO index and a significant relationship is confirmed (Table 7.2 and Figs. 7.8c-d). The model results indicate a more frequently positive IOD index under QBOW and a negative index for QBOE, and these differences are statistically significant in September and October. The GC3 N96-pi and UKESM-pi results are very similar (Fig. S3) and the differences are also significant. The IOD event frequency is also markedly different depending on the QBO phase, with positive events more frequently observed in the westerly phase of the QBO and negative events found more frequently under QBOE, both for ERA5 and the model simulations (Table 7.2).

This section demonstrates statistically robust links between the IOD and ENSO, and the QBO. ENSO and the IOD are intertwined with pan-tropical teleconnections through zonal circulations (Cai et al., 2019), monsoons and the ITCZ. For that reason, the following section explores more closely the links between the QBO and features of the tropical circulation.

7.3.4 ITCZ, monsoons and the tropical circulation

This section investigates how the ITCZ, monsoons and the Walker circulation are influenced by the QBO in the model compared to the observations. Climate model biases in the representation of the migration and dynamics of the ITCZ, or in the mean-state of the Walker circulation, may modify any physical effects of the QBO over convection. For

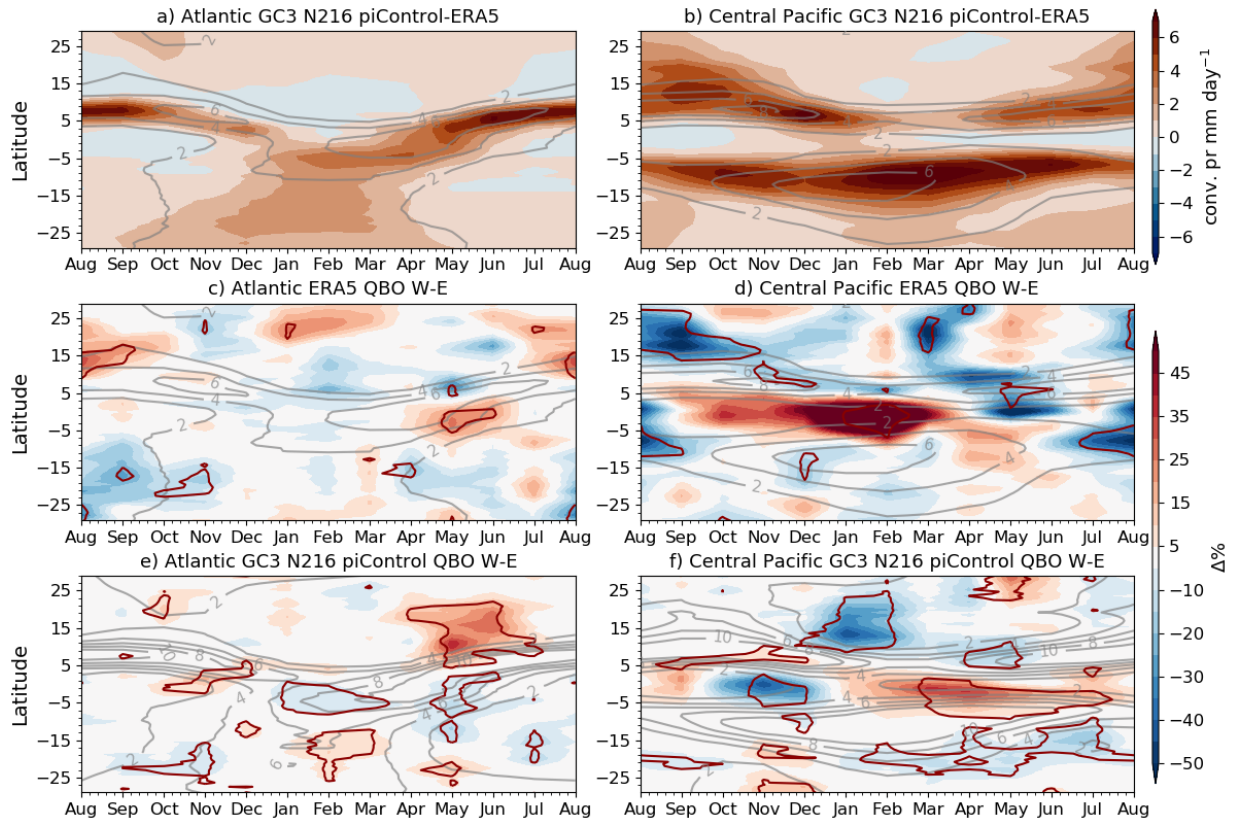


Figure 7.10: (a, b) Zonal mean biases in convective precipitation in GC3 N216-pi compared to ERA5 in the (a) Atlantic [60°W - 20°W] and (b) Central Pacific [180°W - 140°W] sectors. (c-f) Monthly and zonal mean QBO W-E percent (%) differences in convective precipitation where the absolute difference is weighted by the climatological value at each latitude and month. The line-contour (red) depict differences that are statistically significant to the 95% level according to a bootstrapping test and the grey lines show the climatological values.

example, ITCZ biases in position or strength (Fig. 7.10a-b) are noteworthy in the model, and are mainly characterized by a southward shift of the simulated Atlantic ITCZ in DJF and MAM and a wider extent of the Central Pacific ITCZ compared to ERA5.

The monthly-mean QBO W-E zonal-mean convective precipitation differences in the Pacific and Atlantic ITCZ regions (Figure 7.10) show that the ITCZ impacts are seasonally dependent. While there are no clear differences in the Atlantic sector for ERA5 in any month, in GC3 N216-pi there is a significant northward shift of the ITCZ from April to June, which is likely associated with the warm SST anomalies found in this season in the northern tropical Atlantic (Fig. 7.4).

The differences in the Pacific sector confirm previous model and observational results

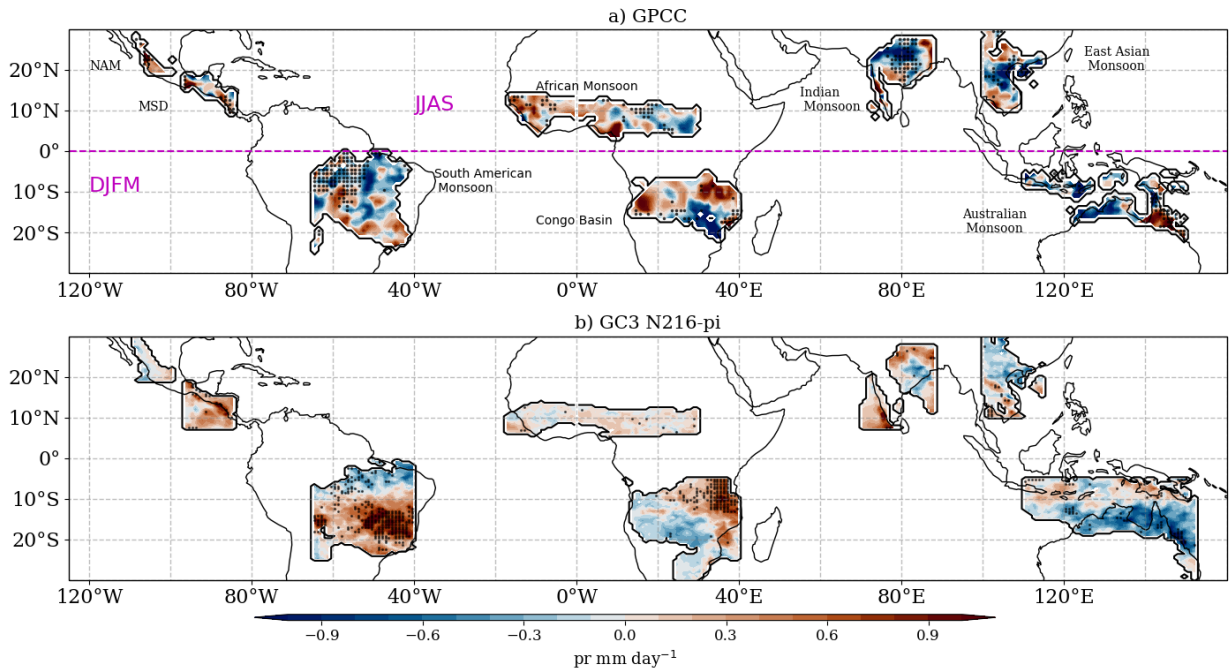


Figure 7.11: Convective precipitation differences in monsoon regions between QBO W-E phases for a) ERA5 and b) GC3 N216-pi. For monsoon regions in the Northern hemisphere, differences are shown for the JJAS period, whereas for Southern Hemisphere monsoons, results are shown for DJFM. Red dots indicate differences that are statistically significant to the 95% level according to the bootstrapping test.

(Gray et al., 2018; Serva et al., submitted) that the Pacific ITCZ becomes stronger and shift southward during QBOW compared to QBOE (Fig. 7.10d, f). In observations, the strongest differences are found during DJF, characterized by increased precipitation over the core ITCZ regions. In GC3 N216-pi, a southward shift of the ITCZ is observed from February to July, maximized in the MAM season. Very similar results for the Atlantic and Pacific sectors were observed for the other two simulations (not shown). The result also holds for ENSO Neutral periods (Fig. S4) which rules out the possibility that the Atlantic ITCZ results are due to ENSO teleconnections to the tropical north Atlantic.

In spite of existing observational evidence (Collimore et al., 2003; Liess and Geller, 2012; Gray et al., 2018) that suggests a link between the QBO and monsoon regions, the results in the previous sections (Fig. 7.2) show little-to-no effect of the QBO on precipitation over land in the simulations. The precipitation response over land is examined more closely by analysing regions that fit the concept of the global monsoon. For this purpose, a monsoon

region is defined as a region in which over 55% of the total annual rainfall is observed or simulated in the respective summer season and the summer-winter rainfall rate difference is higher than 2 mm day⁻¹ (Wang and Ding, 2008; Wang et al., 2017, 2021).

After defining these regions, the QBO W-E differences are computed for JJAS and DJFM for Northern and Southern Hemisphere monsoons, respectively. Figure 7.11 shows that there is no coherent response to the QBO phase in GPCC in any monsoon region. However, in GC3 N216-pi there are significant differences for Southern Hemisphere monsoons. In the South American monsoon region, the QBO W-E differences indicate a significantly wetter region in South America, where the South Atlantic Convergence Zone is located (Carvalho et al., 2004; Jorgetti et al., 2014). Similarly, a drier Australian monsoon and wetter conditions for East Africa are observed during QBOW compared to QBOE.

For Northern Hemisphere monsoons there are no robust or significant differences (Fig. 7.11b). However, when only Neutral ENSO months are considered, all three simulations suggest a wetter Central American monsoon (not shown) in QBOW compared to QBOE. The different responses observed for the three simulations suggest that the representation of the dynamical features of each monsoon by each model configuration is important for any response to the QBO. Furthermore, the relatively smaller signals seen over land compared to over the oceans suggests that SST feedbacks are important for the QBO response in the model, so that reduced impacts are seen in regions of land convection.

A number of studies have suggested a link between the QBO and the Walker circulation to explain the zonally asymmetric nature of the QBO anomalies in convective precipitation (e.g. Collimore et al., 2003; Liess and Geller, 2012). To evaluate this hypothesis, the zonal streamfunction is used to measure the Walker circulation (Yu and Zwiers, 2010; Bayr et al., 2014) and is defined as:

$$\psi = 2\pi \frac{a}{g} \int_0^p u_D dp, \quad (7.5)$$

where ψ is the zonal streamfunction, u_D is the divergence part of the zonal wind, a is the Earth's radius, p is the pressure coordinate and g the gravitational constant. The

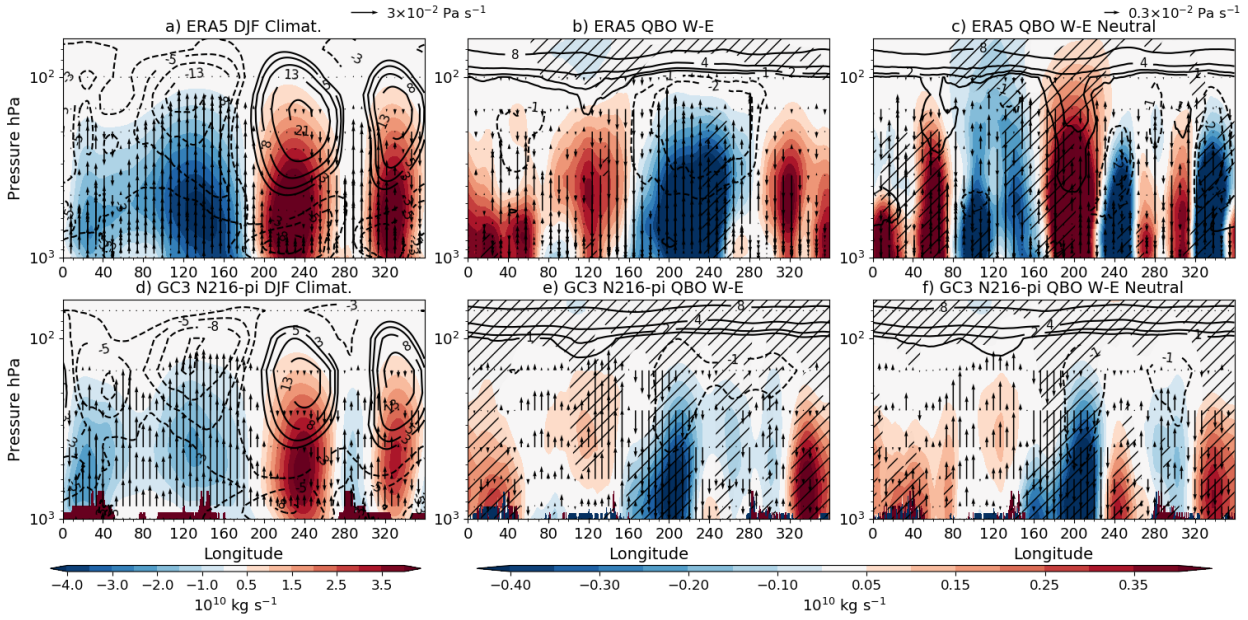


Figure 7.12: (a, d) Climatological mean-state of the Walker circulation, depicted through the zonal streamfunction (ψ) in shading, the zonal wind (contours), and vertical velocity (ω [Pa s^{-1}], vectors) during the DJF season in a) ERA5 and (b) N216-pi. (b, c, e, f) show W-E composite differences, during DJF, for the same variables only that hatching represents statistical significance to the 95% confidence level for differences in the streamfunction, and only statistically significant differences in the zonal wind and ω are shown. (g-h) are as in (d-f) but considering Neutral ENSO periods only. Example vector sizes for ω are given in the top right corners of a and c.

streamfunction is calculated by first averaging over the equatorial band of 10°S - 10°N and integrating to the top level of each dataset.

QBOW minus QBOE composite differences in DJF show that the streamfunction in the eastern Pacific [220-260°E] is significantly weaker during QBOE than during QBOW in ERA5 and GC3 N216-pi (Fig. 7.12). These streamfunction differences are significant even low in the troposphere in the model. The zonal wind at upper-levels (300-100 hPa) is also weaker in QBOW compared to QBOE at 200°E in both model and reanalysis. In GC3 N216-pi, the negative ψ difference is accompanied by descending motion anomalies in the 170-220°E region, whereas anomalous ascent is observed in the Maritime continent and Indian Ocean. The differences in the other simulations agree with the results of GC3 N216-pi (not shown).

In boreal fall (Fig. 7.13), the differences are also significant and are linked to the relationships found between the IOD and the QBO. Specifically, significant positive differences in the streamfunction are found in the eastern Indian Ocean and maritime continent and

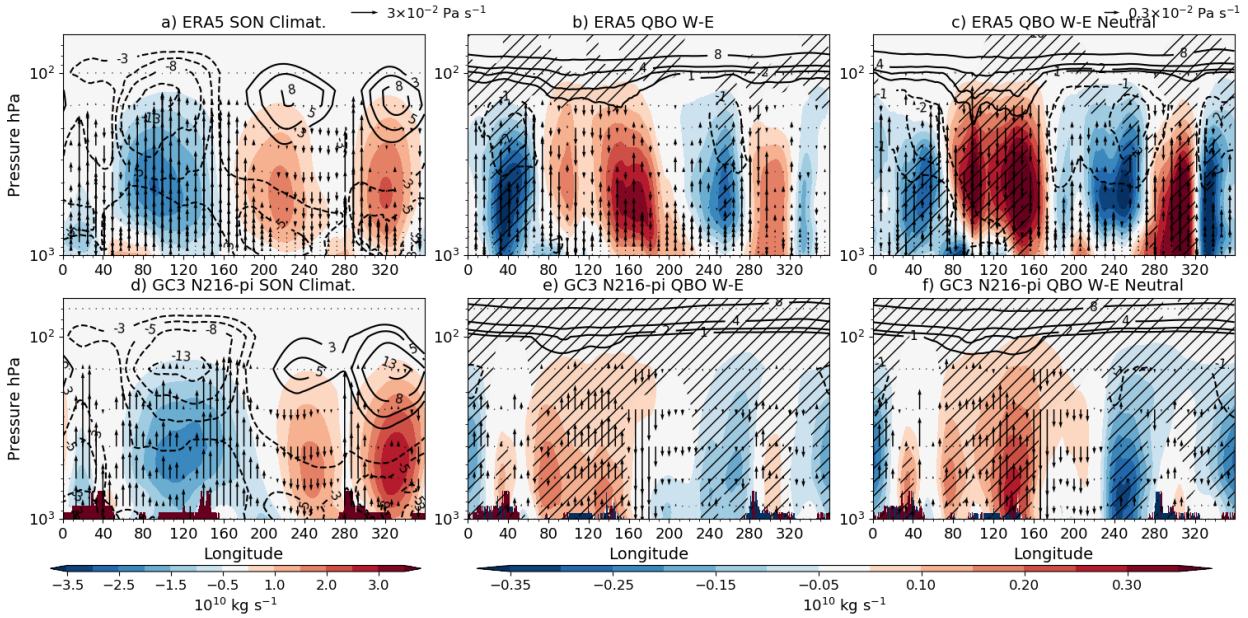


Figure 7.13: As in Figure 7.12 but for the SON season.

negative differences in the eastern Pacific. In GC3 N216-pi, vertical velocity anomalies indicate stronger ascent in the western Indian Ocean and in the Maritime continent whereas descending anomalies are found in the eastern Indian Ocean. These results agree with positive IOD indices found in QBOW and a mean negative index during QBOE.

The rightmost panels in Figures 7.12 and 7.13, in which only Neutral ENSO months are considered, suggest that this relationship between the QBO and the Walker circulation occurs regardless of ENSO events for GC3 N216-pi. However in ERA5, removing ENSO events changes the sign of the response, likely due to the small sample size in the observational record when only neutral months are considered. These results highlight links between the large-scale overturning circulation and local responses which may explain the zonally asymmetric results found in previous studies and in early sections of this chapter.

7.4 The nudging experiments

This section investigates the results from the nudging experiments described in section 7.2.4, in which the zonal wind was relaxed towards ERA5 between 10°S-10°N and 90 and 4 hPa. Before the analysis of the surface response, the QBO W-E variability in the UTLS temperature and zonal wind (Figure 7.14) is larger in the nudged experiments compared to

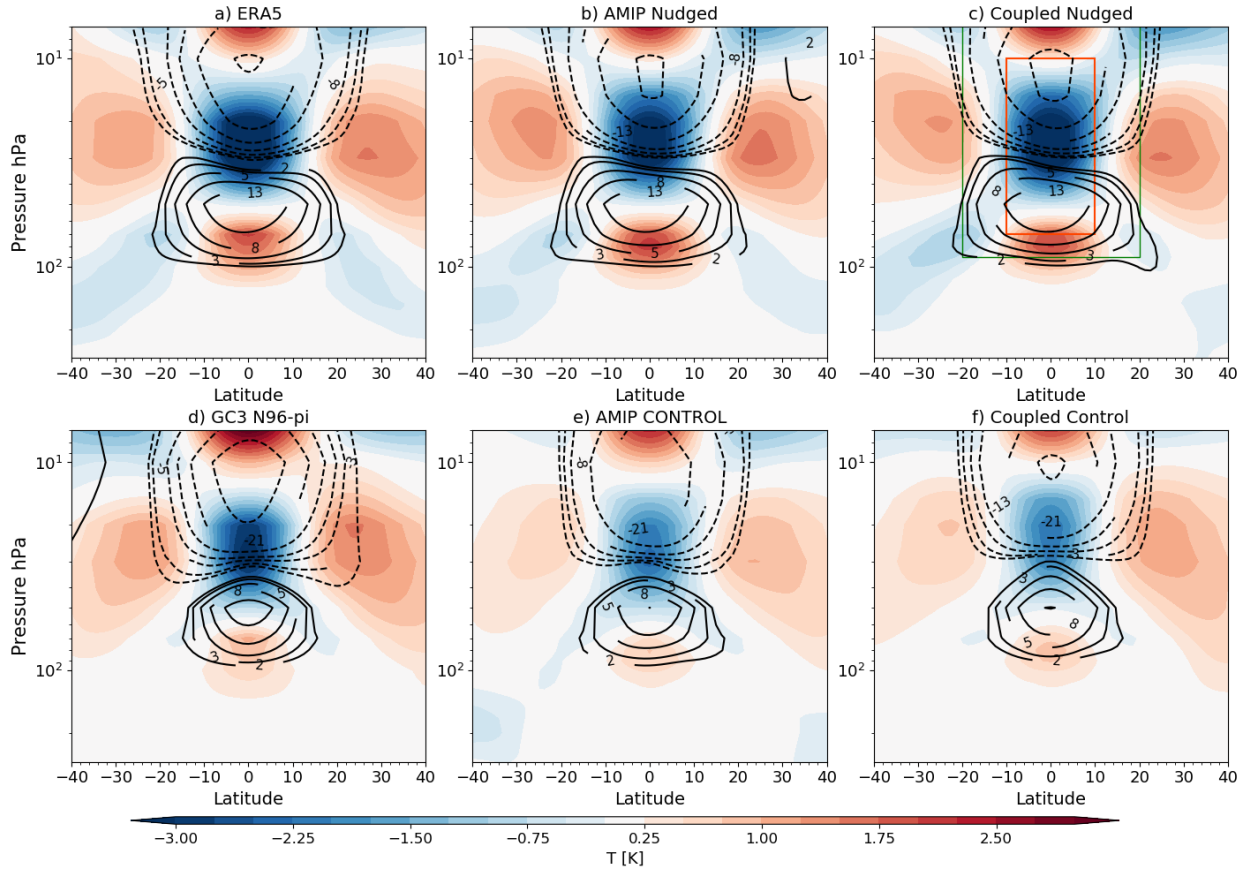


Figure 7.14: Latitude-height plot of the zonal-mean temperature (shading) zonal wind (contours in m s^{-1} differences (QBO W-E) in (a) ERA5, the nudged simulations in (b) AMIP and (c) coupled configurations and (d) GC3 N96-pi from CMIP6, the control simulations with no nudging in an (e) AMIP and (f) coupled configurations, and . The black line denotes the tropopause height obtained from the model data in (b, d) and for ERA5 the tropopause height was found through the gradient threshold method. For the nudged experiments, the ensemble-mean is shown. The nudging region is illustrated in c), where the red box indicates where the full nudging is applied and the green box illustrates the tapered region.

Control experiments which validate the experimental setup. The UTLS variability in the nudged experiments very closely resemble the results of ERA5, particularly in the equatorial region, which suggests that the weak QBO amplitude bias in the lower-stratosphere has been removed by nudging. The removal of the weak QBO amplitude bias means that these nudged experiments are suitable to investigate the surface response to the QBO because in these experiments there is no upward influence from the troposphere to the stratosphere, and the UTLS temperature variability is larger than in free-running simulations, which means that the static stability hypothesis for the tropical route of QBO teleconnections

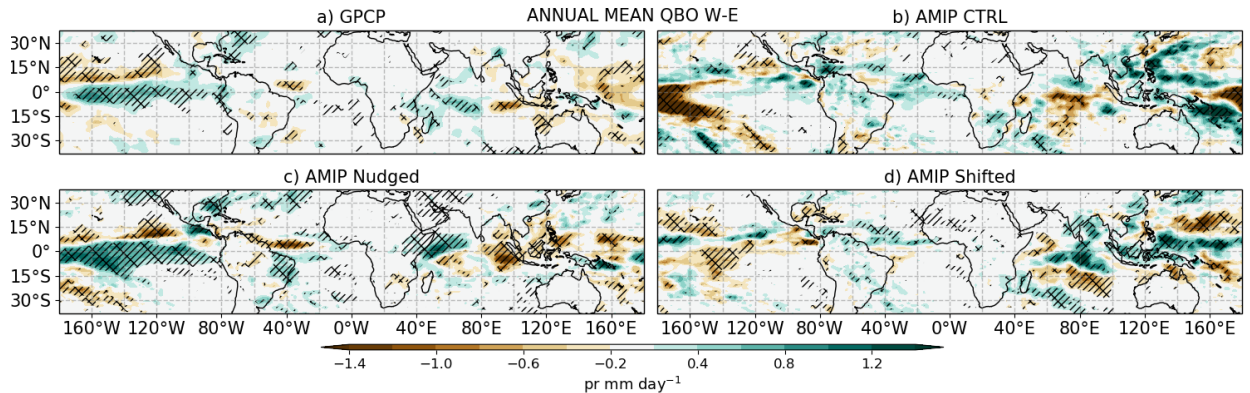


Figure 7.15: Annual-mean precipitation response (QBO W-E) in (a) GPCP, and atmosphere-only experiments: (b) AMIP CTRL, (c) AMIP Nudged and (d) AMIP Shifted.

can be tested through these idealized experiments.

7.4.1 Atmosphere-only experiments

This section describes the results of the atmosphere-only experiments: AMIP Nudged, AMIP Control and AMIP Shifted. First, the precipitation and OLR response is diagnosed. The annual-mean difference of precipitation between W and E phases (Fig. 7.15) in the AMIP Nudged ensemble-mean matches closely the results of GPCP, characterised by an El Niño pattern in the Pacific Ocean, a weaker Atlantic ITCZ and a zonal gradient of precipitation in the Indian Ocean (the IOD) during QBOW compared to QBOE. In contrast, the AMIP Control and the simulations with an out-of-phase relaxation of the winds with respect to the SST driving data (AMIP Shifted) show very different responses to the AMIP Nudged experiment and observations. A similar result is found for seasonal-mean composite differences (not shown), so that the precipitation response in the simulations where the QBO index and the SSTs match exactly as in observations (AMIP Nudged) produce a very similar response to GPCP, whereas simulations where the nudged QBO winds do not match the observed SSTs (AMIP Shifted) result in entirely different responses.

These results mean that the variability of precipitation does not seem to be affected by the nudging. Moreover, nudging does not significantly modify the simulated OLR (Fig. 7.16). The time-series of equatorially averaged OLR (Fig. 7.16a) is indistinguishable between the three types of atmosphere-only experiments and similar results are found

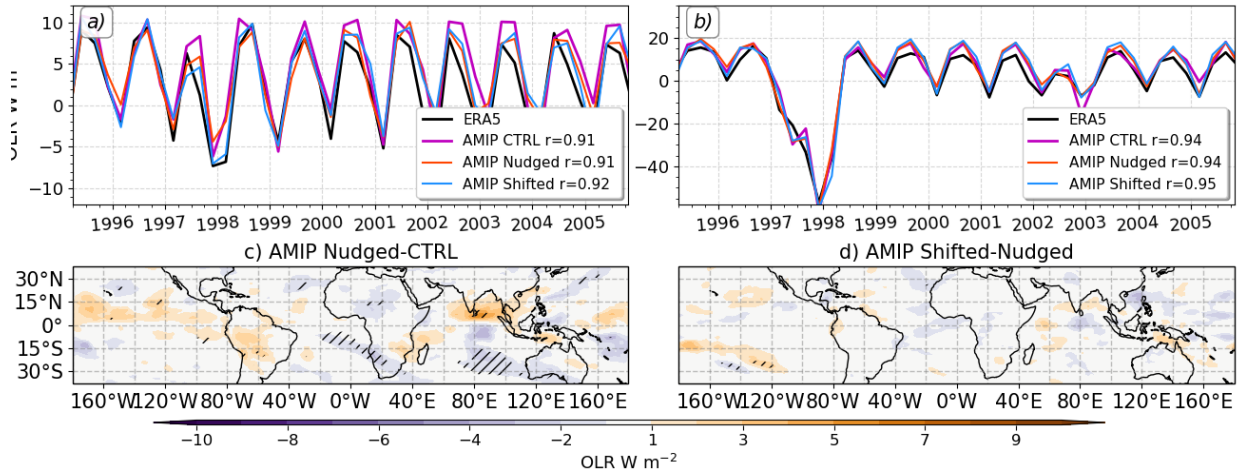


Figure 7.16: (a, b) Time-series of (a) zonal-mean equatorial [5°S - 5°N], and (b) area-averaged EN3.4 OLR in ERA5 and the three amip experiments. For each AMIP experiment the Pearson correlation coefficient between the experiment time-series and ERA5 is shown in the legend. (c) Differences in mean OLR between AMIP Nudged and Control and (d) between AMIP Shifted and Nudged. Significant (95% confidence level) differences according to a Mann-Whitney U test in (c, d) are highlighted with hatching.

for OLR averaged in the EN3.4 region (Fig. 7.16b). The correlation coefficients of the time-series also indicate no difference between the experiments. Similarly, the horizontal distribution of the mean OLR also shows no robust differences between the Control, Nudged and Shifted experiments (Fig. 7.16c-d) so there is no effect of nudging for the mean state or variability of OLR in AMIP experiments.

The analysis of the effect of nudging on the overturning circulation shows that the Walker circulation biases in the upper troposphere of the control experiments are notably improved in the nudged experiments (Fig. 7.17). The mean state of the Walker circulation is weaker in the AMIP Control simulation and exhibits an easterly bias at upper levels compared to ERA5. These two tropospheric biases are improved in the lower stratosphere in the Nudged experiments compared to control experiments.

Even though the relaxation is only applied above 90 hPa, significant differences between control and nudged experiments are observed for the zonal wind and zonal streamfunction at 200 hPa near the dateline, over South America and over the Atlantic Ocean. However, no significant differences in the streamfunction or zonal wind in the lower troposphere are observed between the AMIP Shifted and Nudged experiments which means that

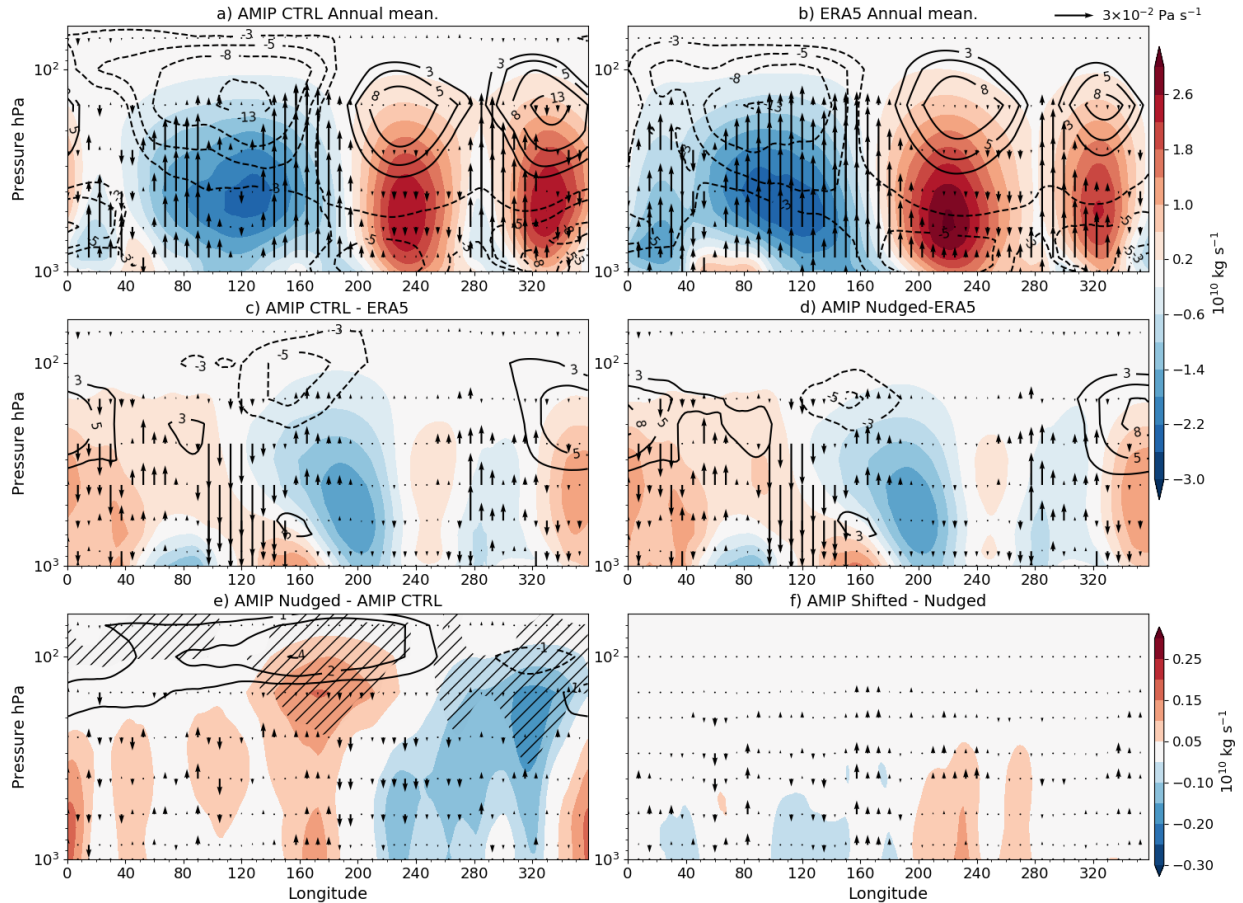


Figure 7.17: Zonal mass streamfunction (ψ in shading), zonal mean zonal wind (contours) and vertical velocity (vectors) averaged over the band 10°S - 10°N . Climatological mean in the (a) AMIP Control experiment and (b) ERA5. (c-d) show biases in the (c) Control and (d) Nudged experiments with respect to ERA5 whereas (e-f) show differences between experiments, (e) AMIP Nudged-Control and (d) AMIP Shifted-Nudged. Note that the colorbar and scale of the vectors changes are different between (a-d) and (e-f). In (e-f), significant differences (95% confidence level according to a Mann-Whitney two-sided test) in the streamfunction are highlighted with hatching.

the mean overturning circulation is not modified by the variability of the nudging data, only by the mean-state of the nudging data. These results mean that even though the upper troposphere is affected by the nudging, the surface precipitation and the OLR are independent from the QBO winds.

This section shows that the nudged experiments have a better representation of the stratospheric variability in temperature and vertical wind shear; however, the precipitation response associated with the QBO variability is entirely different between AMIP Nudged and Shifted experiments, with the difference between these two experiments being the

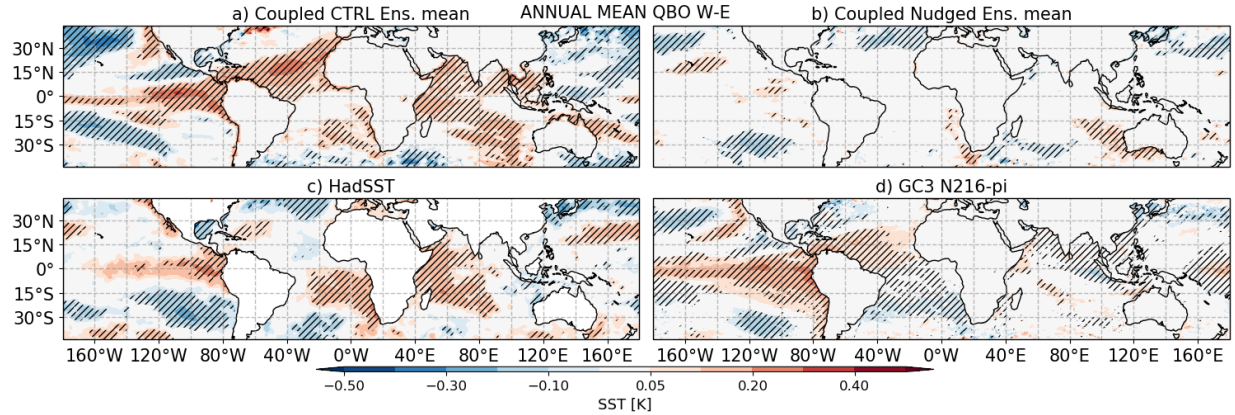


Figure 7.18: Annual mean SST [K] QBO W-E differences in (a) Coupled Control and (b) Coupled Nudged ensemble mean, and the (c) HadSST dataset and (d) GC3 N216-pi datasets. Hatching denotes significance to the 95% confidence level according to a bootstrapping with replacement test.

underlying SSTs. These results suggest that the QBO winds, and the effect of the nudging on the upper-tropospheric winds, are secondary to the effect of the SSTs for the precipitation response in these atmosphere-only experiments. In other words, in these experiments the surface response of precipitation is largely associated with the underlying SSTs and not the QBO winds. However, whether there is any feedback mechanism between the QBO and SSTs cannot be answered by this atmosphere-only configuration, which leads to the next section which analyses the coupled nudged experiments.

7.4.2 Coupled experiments

This section presents the results of the coupled ocean-atmosphere experiments, comparing the experiments with nudging (Coupled Nudged) in the tropical stratosphere and without (Coupled Control). Note that all the individual experiments in this section are the same length (35 yr) and that the Coupled Nudged ensembles size is six and the control ensemble is composed of two members.

First, differences in SSTs are analysed given that the previous section shows that the SST forcing dominates over the nudging in atmosphere-only experiments. The annual mean QBO W-E difference in tropical SSTs (Fig. 7.18) in the coupled control experiments is very similar to the response of HadSST and GC3 N216-pi. These QBO W-E responses in the

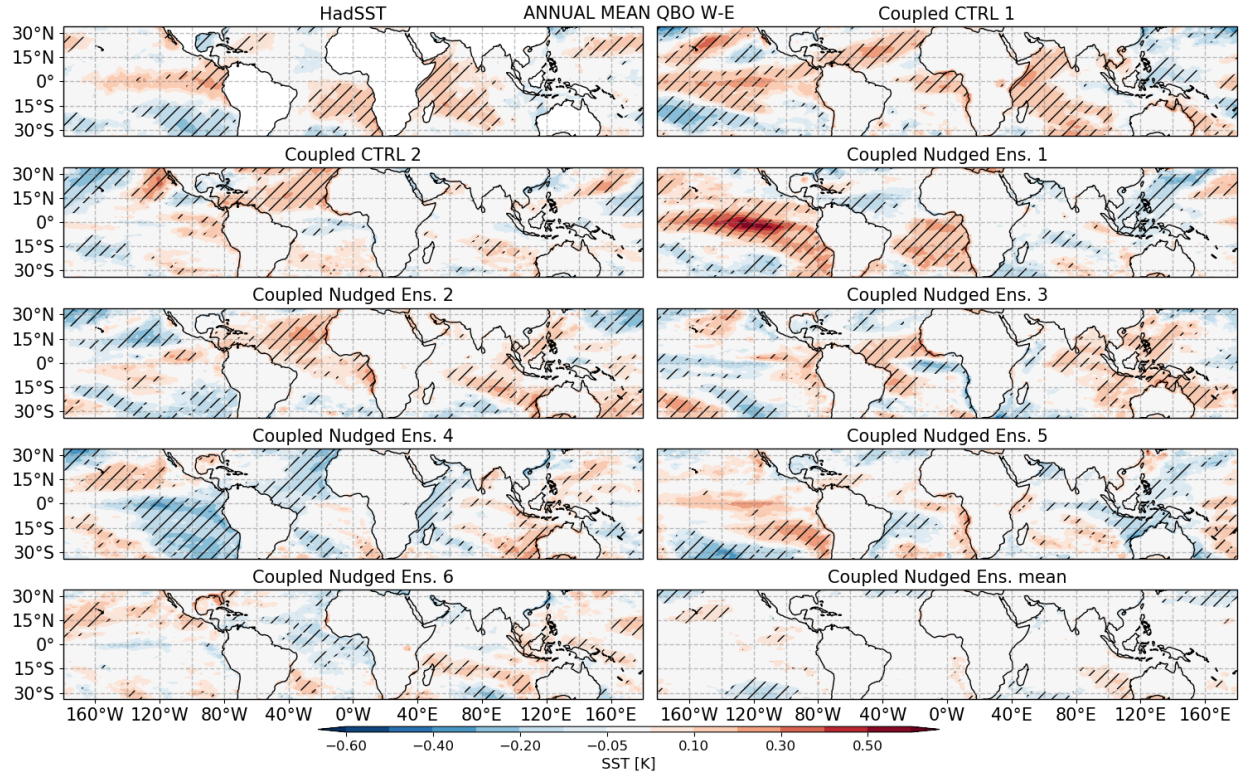


Figure 7.19: Annual-mean SST differences between QBO phases in the HadSST, Coupled Control and Coupled Nudged simulations.

control experiments and HadSST datasets are characterized by warm signals in the East Pacific, and the northern tropical Atlantic and Indian Oceans.

The nudged ensemble-mean, however, shows a very weak or null response (Fig. 7.18b) compared to the control experiments. The ensemble-mean weak response is a result of very different responses from each ensemble member (Fig. 7.19) which cancel each other out to a large extent indicating that internal variability is larger than the QBO effect in the simulations with a nudged QBO. In seasonal-mean differences the SST response also appears to be stronger in the tropics in the free-running Coupled Control experiments than in the nudged experiments (not shown). These results suggest that SST differences diagnosed in two types of control simulations are missing when the nudging is implemented.

The precipitation response is also weaker when the nudging is applied to the coupled configuration simulations. The annual mean difference between QBO phases (Fig. 7.20) in the control experiments show two significant QBO W-E differences: a significant El Niño-like response over the Central and Eastern Pacific Ocean, and a wetter western

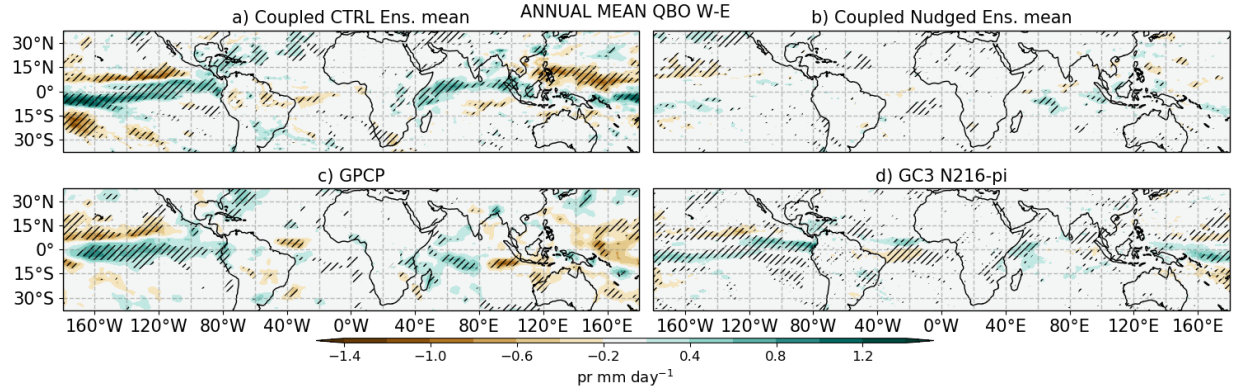


Figure 7.20: As in Fig. 7.18 but for precipitation [mm day^{-1}] using (c) GPCP as the observational dataset.

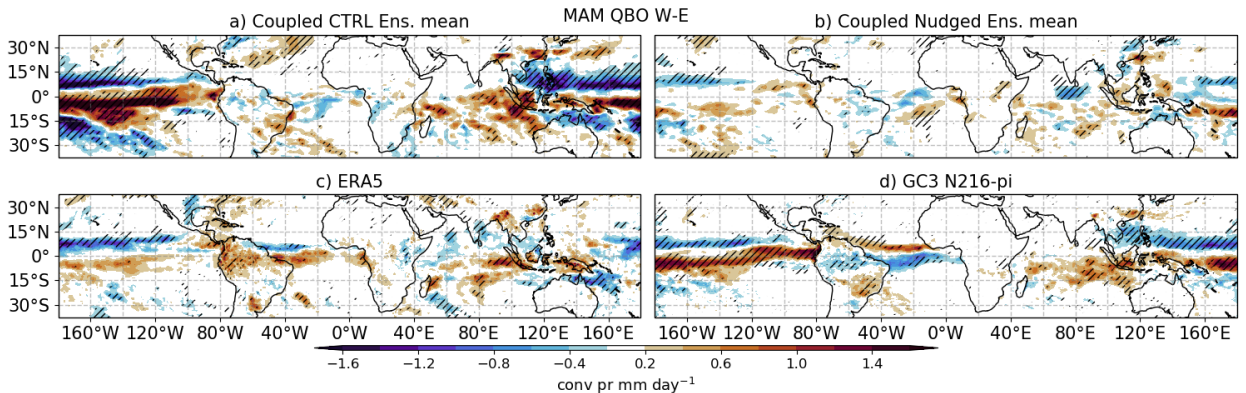


Figure 7.21: As in Figure 7.20, but for the MAM season and convective precipitation.

Indian Ocean. These two precipitation responses are also observed in GPCP and GC3 N216-pi. The ensemble-mean of the nudged experiments, however, shows no robust or region-wide significant differences (Fig. 7.20b).

The weaker response in the ensemble-mean of the nudged experiments is also due to opposite responses found in each ensemble member which cancel out. In specific seasons, robust QBO W-E responses in convective precipitation are observed in the Control experiments, ERA5 and GC3 N216-pi, for example, a meridional dipole in the Pacific Ocean (Fig. 7.21) and a wetter eastern Indian Ocean. These results confirm that the control experiments exhibit QBO-related precipitation impacts similar to those found in the CMIP6 experiments and in some instances also similar to the observed impacts. However, these precipitation anomalies disappear in the nudged experiments.

Robust relationships between the QBO phase, and IOD and ENSO indices are observed

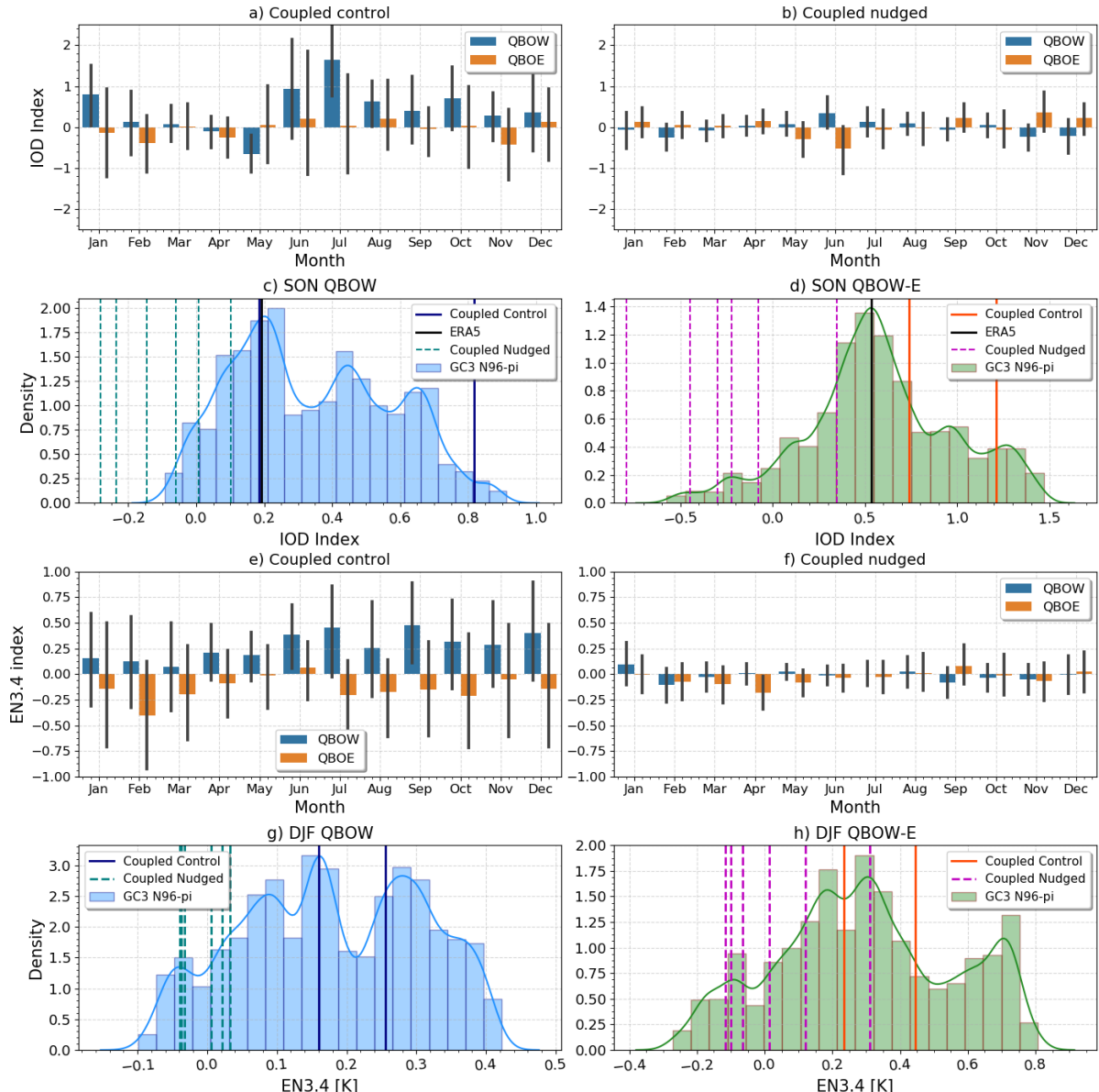


Figure 7.22: (a, b) Monthly-mean convective precipitation IOD index [mm day^{-1}] in coupled (a) control and (b) nudged ensemble-means separated by QBO phase. (c, d) Probability density functions (PDFs) of the IOD convective precipitation index for (c) the mean SON during QBOW months and (d) the SON difference between QBO W-E. The PDF is obtained from the 500 yrs of the GC3 N96-pi by bootstrapping 10,000 times into 35-yr periods and obtaining the averages and differences in each subsample. (e-f) as in (a, b) but for monthly-mean EN3.4 index [K] in the ensemble mean (e) Coupled control and (f) Coupled Nudged simulations separated by QBO phase. (g-h) as in (c-d) but for the EN3.4 index in DJF.

in the CMIP6 experiments (see section 7.3.3). Figure 7.22 shows the mean values of ENSO and IOD indices for nudged and control experiments. Coupled control experiments (Figs. 7.22a, e) show a significant difference for both IOD and ENSO indices identical to the CMIP6

results, i.e., both indices tend to be positive under QBOW and negative under QBOE. For the IOD index, these differences are observed from Jul-to-Jan and for ENSO the differences are found almost year-round but are stronger during boreal fall and winter. However, the nudged ensemble-mean shows no relationships between these indices and the QBO phase.

The long CMIP6 picontrol simulations were analysed by computing QBO W-E differences of the indices for 35-yr long randomly selected periods iteratively 10000 times. [The selection of 35-yr periods is to match the length of the observed period in order to investigate how likely is it to find a QBO W-E difference value if the piControl simulations were of the same length as observations.](#) This approach leads to a probability density function (PDF) of QBO W-E differences that aims to sample the role of internal variability within the long piControl integration on the QBO differences and to evaluate how these coupled experiments fit within those distributions with and without nudging.

Figure 7.22d, for instance, shows that the QBO W-E differences in the SON IOD index are predominantly positive in the GC3 N96-pi distribution, and the differences in the two ensembles members of the control experiment are positive as well. However, the Coupled Nudged ensemble members are mostly negative and two of them fall outside the 99% low end of the PDF. The EN3.4 index is also more frequently positive under QBOW (Fig. 7.22g) than under QBOE in the CMIP6 and control experiments. There seems to be some indication that the response in the nudged experiments averages to 0, which is still likely in the GC3 N96-pi PDF.

This section shows that in the coupled configuration experiments there are notable QBO-related impacts that are removed when nudging is applied to the model. In the control experiments, impacts over the ITCZs, ENSO and the IOD, to name a few, are robust and similar to results from observations and CMIP6 integrations of the model. However, in the nudged experiments, little-to-no robust responses were observed, as each ensemble member exhibited a different response, leading to a cancellation of the differences in the ensemble-mean. The implications of these results for the stratospheric-tropospheric coupling and QBO teleconnections is discussed in the following section.

7.5 Summary and discussion

Analyses of observational records of precipitation have long suggested links between the stratospheric QBO and deep tropical convection (Collimore et al., 2003; Liess and Geller, 2012; Gray et al., 2018). However, the short available observational record (<40 years) and the confounding influence of ENSO and its teleconnections limits the robustness of any analysis seeking to explore these links and possible mechanisms of interaction between the QBO and tropical surface climate. The first part of this chapter investigates the tropical signature of the QBO in 500-year-long pre-industrial control CMIP6 experiments, with a focus on the HadGEM3 GC3.1 N216 simulation.

Composite and regression analyses were used to demonstrate the presence of a statistically significant link between the QBO and several tropical climate features. During QBO W relative to QBO E, there is a strengthening of the East Pacific ITCZ and a drier SACZ area in boreal winter, a northward shift of the Atlantic ITCZ and a wetter Caribbean Sea in JJA and a strong dipole signal in the Indian Ocean in SON. The QBO signal was found to be zonally asymmetric, with the more robust and largest differences over the oceans, suggesting the possibility of SST feedback processes. The modelled QBO signals agree well with observational analyses and the length of the simulation allows for improved estimation of statistical significance and further exploration of the possible source of these signals.

The possibility of aliasing of the QBO and ENSO signals and their interaction was extensively explored, using the model simulations. When only ENSO-neutral years are analysed the QBO signal remains essentially unchanged, ruling out the possibility of a straightforward aliasing of ENSO events with the QBO phase selection. The possibility that the apparent QBO signature at the surface is due to an ENSO bias in selection of the QBO phase was also considered. An influence of ENSO on the descent rate and amplitude of the QBO, via modulation of tropical wave generation, has been proposed (Schirber, 2015). However, while the model was found to successfully simulate the well-known difference in QBO descent rates in which the QBOW phase descends more rapidly than the QBOE phase, there was no evidence for an ENSO influence on the rate of descent or amplitude of either QBO phase.

This analysis therefore provides evidence for a QBO influence on tropical surface climate that is not simply due to aliasing or a bias in how the QBO index is determined. However, the QBO response patterns strongly suggest that any QBO influence is likely to involve processes such as deep convection and tropical circulation patterns that are also influenced by ENSO. Potential pathways of interaction between the QBO and ENSO signals were therefore explored. While recognising that linear diagnostics are unable to provide specific evidence of cause and effects, they may nevertheless identify candidate mechanisms that are worth exploring more fully.

The frequency of ENSO events in each phase of the QBO was first explored. In observations, El Niño events have been found to occur more frequently in QBOW years and La Niña events are more frequently found in QBOE years (Taguchi, 2010), suggesting a non-linear interaction of ENSO with the QBO. This dependence was successfully reproduced in the model, providing supporting evidence that the observed QBO-ENSO relationship is not due to observational uncertainty. Similarly, examination of month-by-month ENSO amplitude and interannual variability in the model showed that the interaction between QBO and ENSO is far from linear, since the amplitude dependence on QBO phase was asymmetric. The non-linearity of the QBO-ENSO interaction was confirmed using composites that showed different QBO signal patterns during El Niño years compared with La Niña years.

In addition to the QBO-ENSO link, the model analysis of total precipitation also highlighted a statistically significant QBO signal in the Indian Ocean, raising the possibility of an interaction with the Indian Ocean Dipole (IOD). In boreal fall the IOD index, which measures the zonal gradient of precipitation in the Indian Ocean, was found to be anomalously positive in QBOW years and anomalously negative in QBOE years.

Finally, this chapter confirms the previously proposed hypothesis that the QBO may influence the mean-state of the Walker circulation, which could explain the zonally asymmetric nature of the QBO signal in precipitation in the tropics (Collimore et al., 2003; Liess and Geller, 2012; Hitchman et al., 2021). The modelled Walker circulation was found to vary by up to 10% between QBO phases, even when the effect of ENSO events was taken into account. Specifically, the Walker circulation was found to be weaker during QBOW than during QBOE. In DJF, this anomaly of the overturning circulation in the Pacific is likely

linked to the stronger East Pacific ITCZ, and in SON, the changes to the Walker circulation are likely linked to the ascending and descending motions that characterize the IOD.

These results are amongst the first robust pieces of evidence of QBO-tropical convection signals in a GCM. However, the methodology used does not allow to conclusively separate the cause-effect of the diagnosed relationships. For example, these relationships could be explained by anomalous tropical wave activity that may shift the QBO phase to a preferred state, but, e.g., there was no evidence of an influence by ENSO on the downward propagation or amplitude of the QBO.

Alternatively, a top-down influence of the QBO in the tropics could explain these results. Several hypotheses have been put forth to explain a causal link between the QBO and tropical convection (Hitchman et al., 2021; Haynes et al., 2021) and the most prominent hypothesis suggests that UTLS temperature variability modifies the upper-level static stability to the extent of affecting the height and strength of convection. However, models including GC3 N216-pi underestimate the effect of the QBO on the UTLS static stability and may therefore also underestimate the impact of QBO teleconnections in the tropics.

For that reason, atmosphere-only and coupled ocean-atmosphere experiments were conducted with the model stratosphere relaxed towards ERA5 in the QBO region. These experiments notably improve the QBO amplitude in the lower stratosphere and simulate a stronger impact of the QBO on the UTLS static stability. One could have reasonably hypothesized that stronger surface impacts would be observed in the nudged experiments relative to the control experiments.

The results from the AMIP experiments shows that the nudging modifies the upper-level branch of the Walker circulation, yet the nudging makes little-to-no difference over the equatorial surface precipitation or OLR, suggesting a possible role for SST feedbacks. In fact, the coupled control experiments reproduce all the impacts diagnosed in the first part of the chapter. However, the SST and precipitation responses appear to be removed in the coupled nudged experiments. Individual ensemble members of the simulations with nudging show significant responses but the ensemble-mean response is null. Furthermore, the diagnosed relationships of the QBO with ENSO and the IOD in the CMIP6 models, which are also found in the control experiments, disappear in the nudged experiments.

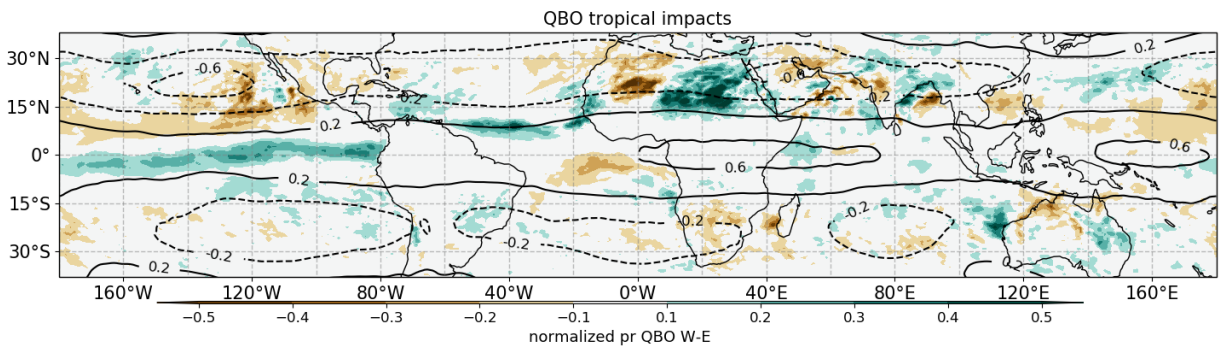


Figure 7.23: Summary of the UTLS static stability mechanism for QBO teleconnections to tropical precipitation. QBO W-E differences in air temperature at 100 hPa (contours) and precipitation normalized by the climatological values (shading) for the GC3 N216-pi simulation in the SON season.

The results from the nudging experiments can be interpreted in various ways. First, since the experiments in which the influence from the troposphere to the stratosphere was removed by nudging the stratosphere in the model show no surface response, one could reasonably conclude that there is no downward tropical route of the QBO. Similar questions have arisen regarding the MJO-QBO relationships with some studies suggesting that there is no causal link, and the observed relationship is a result of statistical effects (Wang et al., 2019).

A second plausible explanation is that the UTLS static stability mechanism is not the causal pathway through which the QBO influences the tropical troposphere. Several lines of evidence in this chapter seems to contradict the predictions of the UTLS static stability mechanism. For instance, results from the first part of the chapter show zonally asymmetric responses that appear in all seasons and a clear difference in the magnitude of the impacts over ocean than over land.

The UTLS static stability mechanism should produce zonally symmetric effects or at least be relevant in all deep convective regions and there is no reason why land monsoon regions should be less affected by the UTLS static stability. Figure 7.23 summarises the arguments against the UTLS static stability mechanism in the results from the piControl experiment by highlighting that the QBO-related differences of temperature at 100 hPa are not collocated with the surface precipitation differences. In South America and Africa, there are strong differences in the 100 hPa temperatures but little differences in precipitation, whereas the Central Pacific shows a similar UTLS temperature variability and a stronger precipitation

signal. Therefore, even in the free-running simulation, the UTLS static stability mechanism does not seem to be the dominant factor but more so in the nudged experiments where the UTLS static stability has a higher QBO-related variance the responses are removed. Therefore, it is possible that other mechanisms that may include feedback processes and that have been muted by the nudging may be at play.

This chapter has therefore proven that robust links exist between the QBO and the tropical troposphere in a state-of-the-art climate model. Nevertheless, the results of this chapter are inconclusive as to the mechanisms that generate this coupling, as experiments with a nudged stratosphere remove these links. If there is no downward stratospheric-tropospheric teleconnection, further research must explain why some robust sensitivity to the QBO phase appears in the model for several convective features.